



HAL
open science

Conductive-radiative heat transfer within SiC-based cellular ceramics at high-temperatures: A discrete-scale finite element analysis

Mohd Afeef Badri, Y. Favennec, Pierre Jolivet, Benoit Rousseau

► To cite this version:

Mohd Afeef Badri, Y. Favennec, Pierre Jolivet, Benoit Rousseau. Conductive-radiative heat transfer within SiC-based cellular ceramics at high-temperatures: A discrete-scale finite element analysis. *Finite Elements in Analysis and Design*, 2020, 178, pp.103410. 10.1016/j.finel.2020.103410 . hal-02944753

HAL Id: hal-02944753

<https://hal.science/hal-02944753>

Submitted on 15 Dec 2020

HAL is a multi-disciplinary open access archive for the deposit and dissemination of scientific research documents, whether they are published or not. The documents may come from teaching and research institutions in France or abroad, or from public or private research centers.

L'archive ouverte pluridisciplinaire **HAL**, est destinée au dépôt et à la diffusion de documents scientifiques de niveau recherche, publiés ou non, émanant des établissements d'enseignement et de recherche français ou étrangers, des laboratoires publics ou privés.

Conductive-radiative heat transfer within SiC-based cellular ceramics at high-temperatures: a discrete-scale finite element analysis

M. A. Badri^{a,*}, Y. Favennec^a, P. Jolivet^b, B. Rousseau^{a,**}

^aCNRS, Laboratoire de Thermique et Énergie de Nantes, 44306 Nantes, France

^bCNRS, Institut de Recherche en Informatique de Toulouse, 31062 Toulouse, France

Abstract

Cellular ceramic materials possess many favorable properties that allow to develop efficient modern-day high-temperature thermal energy conversion systems and processes. The energy conversion within these porous media is governed by tightly coupled conduction–radiation physics. To efficiently design and optimize these systems, a comprehensive understanding of the conduction–radiation behavior within these materials becomes important. In this study, by performing large-scale numerical experiments, we analyze the conduction–radiation coupling characteristics within different (with respect to topology and porosity) SiC-based open-cell cellular ceramics surrounded by fictitious vacuum up to temperatures of 1800 K. To induct minimal approximations, our finite element simulations are based on a discrete-scale approach within which realistic discrete (pore-level) representations of the cellular ceramics are used as numerical media. The results presented in this study provide means to better understand the role of radiation in the coupled conduction–radiation physics within the ceramic samples. A detailed comparison on effectiveness of energy conversion is established for SiC-based full-scale cubic-cell, Kelvin-cell, and pseudo-random-cell ceramic structures which are at 80 % and 90 % porosity each. In conclusion, among the different standalone and full-scale ceramic samples, the Kelvin-cell structures at 90% porosity have proven to benefit the most from radiation coupling.

Keywords: Heat transfer, Conductive–radiative transfer, Open-cell cellular ceramics, Finite element analysis, Discrete-scale approach

1. Introduction

Open-cell cellular ceramics belong to a class of smart materials that are often used as a key element for designing high-temperature engineering systems. Thermal insulation systems [1], porous gas burners [2], volumetric solar power receivers [3], solar thermochemical systems [4], hot gas filters [5], and heat exchangers [6], are few examples of such systems. Involvement of high-temperature physics implicates accurate prediction of heat transport as one of the primary factors for optimizing the global performance of these systems. As such, many researchers have focused on studying (numerically or experimentally) the behavior of open-cell cellular ceramics at high temperatures, especially at temperatures beyond 1200 K [7, 8, 9, 10]. Complementary to these researches, the current article focuses on analyzing coupled conductive–radiative heat transport of topologically different open-cell cellular ceramics up to 1800 K.

By definition, open-cell cellular ceramics are porous materials composed of an interleaved network of ligaments (the solid phase), which encompasses a void phase. Because of their intrinsic material properties, open-cell cellular ceramics offer many distinct advantages over other materials such as metals or polymers. They possess: high strength-to-weight ratio, high specific surface area, good flow-mixing capacity, high thermal shock resistance, and high resistance to chemical corrosion [11]. These set of properties have made open-cell cellular ceramics an attractive choice for designing high-temperature compact systems, examples of which were provided in the preceding paragraph.

To improve the performance of high-temperature systems based on open-cell cellular ceramics, understanding the detailed energy transport involved within such systems is important. The energy transport within most of these devices are due to the coupling between the two main individual modes of heat transfer, conduction and radiation [12]. Because of their microstructure (pore size, wall thickness...), these materials have a complex multiscale texture which actively attenuates thermal transfer via both conduction and radiation. Such a framework explains why engineers and researchers, interested in innovative design of open-cell cellular ceramics, use the time-consuming and expensive trial-and-error iterative design cycle. The reduction of this development

*Present Address: DEN – Service d’Études Mécaniques et Thermiques (SEMT), CEA, Université Paris-Saclay, 91191 Gif-sur-Yvette, France.

**Corresponding author: benoit.rousseau@univ-nantes.fr

Nomenclature

Acronyms

FEM	finite element method
HCE	heat conduction equation
RTE	radiative transfer equation
SiC	silicon carbide
SUPG	streamline upwind Petrov–Galerkin

Symbols

β	extinction coefficient
\mathbf{n}	outward unit normal vector
\mathbf{s}_m	discrete direction vector
\mathbf{x}	Cartesian space coordinates
Γ	interface boundary
γ	SUPG stabilizing coefficient
λ	thermal conductivity
\mathbb{I}	vectorial radiative intensity
\mathbb{R}_R	vectorial reflection operator
\mathbb{V}	vectorial finite element test function
\mathcal{E}	equation
Ω	bounded domain
Ω^h	finite element mesh
ϕ	porosity
ρ	reflectivity
σ	Lattice Boltzmann’s constant
ε	emissivity
G	radiative density

I_m	discrete radiative intensity
k	number of nonlinear iterations
N	conduction–radiation parameter
n	refractive index
N_d	number of discrete directions
Q_r	radiative heat flux
S_v	volumetric surface
T	temperature
T_{s-v}^θ	interface temperature
$T_{s,g+}^\theta$	hot Dirichlet temperature
$T_{s,g-}^\theta$	cold Dirichlet temperature
v	finite element test function
w_m	quadrature weight
x	x -coordinate
y	y -coordinate
z	z -coordinate

Subscripts

D	Dirichlet
eff	effective
in	input
R	reflective
s	solid
v	void

25 time and consequently of the associated manufacturing cost motivates numerical modeling strategies aiming
 26 at accurate predictions of coupled conduction–radiation behavior of open-cell cellular ceramics. Additionally,
 27 for temperatures beyond 1200 K, numerical approaches are decisive for estimating the conduction–radiation
 28 coupling via the effective thermal conductivity [13]. This is because such temperatures are beyond the work-
 29 ing range of current-day experimental facilities (guarded hot-plate, transient plane source, transient hot-wire
 30 technique), often applied for the characterization of effective thermal conductivity [7, 8], or present hardly
 31 exploitable signals (laser flash technique) [14].

32 To numerically study the conduction–radiation coupling behavior within porous media, and consequently in
 33 the open-cell cellular ceramics, two main approaches have been established: the continuum-scale approach and
 34 the discrete-scale approach. The continuum-scale approach consists in modeling the governing heat transfer
 35 equations within an equivalent continuous medium. The approach is often dubbed as the homogeneous phase
 36 approach [15]. As an input, it requires, beforehand, the knowledge of the effective thermophysical quantities
 37 (volume-averaged properties). These properties are either obtained from analytical/empirical relationships,
 38 or are computed [16, 17]. Given the volume-averaged properties, the computations are then carried out in
 39 representative elementary volumes, assuming thermal equilibrium between both solid and fluid phases. When
 40 thermal gradients exist, some authors have introduced a refined method called the multiphase approach that
 41 requires solving a set of two coupled radiative transfer equations [15, 16]. The reason that motivates the
 42 continuum-scale approach is its low computational cost, and that it avoids topological complexities of real-
 43 world porous problems. Undoubtedly, these methods can well predict the overall thermal transport behavior for
 44 the open-cell cellular ceramics. However, the calculation of the exact radiative fields or the exact temperature
 45 field within the volume of the open-cell cellular ceramics is beyond the capabilities of these methods. It may
 46 lead to misunderstanding the real role played by the solid network in terms of its radiative propagation.

47 The second approach, the one used in this communication, is called the discrete-scale or the pore-scale
 48 approach. This kind of approach involves direct pore-scale simulations, while using realistic topological data
 49 (tomographic or virtually generated) of the ceramic skeletons [18, 19]. The generalized heat equation laws are
 50 applied at the microstructure level, i.e, within ligaments and pores. Appealingly, these methods can provide
 51 critical information concerning the conduction–radiation coupling behavior within the bulk of the ceramics.
 52 The method can also be used to identify the energy localization zones within the ceramics. Moreover, in [20],
 53 it was found that at high temperatures (> 1000 K), the discrete-scale approach yielded more accurate results
 54 than the continuum-scale approach. Currently, the method has been drawing considerable attention. However,

55 a major bottleneck of this approach is its computational requirements.

56 In general, the continuum-scale approach remains popular for characterizing the conduction–radiation be-
57 havior of open-cell cellular ceramics. Moreover, for the sake of easiness, the conductive and the radiative
58 contributions are determined separately [18], in a decoupled fashion. One of the simplest ways for performing
59 the radiative calculation is by incorporating the Rosseland diffusion approximation, which assumes that the
60 porous medium can be considered optically thick [12, 13, 21, 22]. Although this approximation allows a qual-
61 itative description of the prominent role of radiation when temperature rises, in many cases, the values can
62 be ill-predicted when compared with experimental data [13, 18]. In fact, summing the conduction and radia-
63 tion heat fluxes neglects the coupling effects, and such a simple addition is only applicable for weakly coupled
64 conduction–radiation physics, i.e., at low temperatures.

65 Alternatively to this simplified superimposing, a more robust approach involves simultaneously considering
66 the divergence both of the conductive and radiative fluxes. Such an approach becomes mandatory for obtaining
67 feasible and reliable solutions. Consequently, in this case, one ends up solving a system of highly nonlinear
68 equations that are tightly coupled. Chen et al. [13] used the spherical harmonics P_1 approximations to solve the
69 radiative heat transfer and the system of equations was finite differenced. Mendes et al. [7] combined the discrete
70 transfer method for the determination of the radiative intensity needed afterwards for estimating the divergence
71 of the radiative flux and the finite volume method for the calculation of the coupled conduction–radiation heat
72 flux. Coquard et al. [14] used the finite volume method for the energy equation and the discrete ordinates method
73 for the radiative transfer equation to approximate the coupled conductive–radiative physics, within the laser flash
74 method. These numerical methods lead to satisfactory predictions of the temperature (globally), but, once again,
75 since continuous scales were used, the prior accurate determination of both the effective thermal conductivity
76 and of the thermal radiative properties was required. According to the choice of the methods (analytical
77 versus numerical) for computing these effective quantities, some discrepancies can be found [18, 23], therefore
78 raising some questions on the accuracy of the continuum-scale approach. Furthermore, the calculation of the
79 exact temperature fields within the volume of the cellular ceramics is beyond the capabilities of these methods
80 whereas this information is crucial for understating the local behavior of other physical properties at high
81 temperatures. Supporting this statement, for standalone radiation physics, in [24] it was shown that the use of
82 realistic tomographic representations for the open-cell porous materials yields results closer to the experimental
83 measurements. It was also recently underlined in [25, 26] that the real microstructure ligament geometries
84 influence at large the radiative physics for the open-cell porous materials. Also, theoretical developments based
85 on upscaling approaches for coupled heat transfer [27], emphasize on the precise prediction of local-scale energy
86 transport which is possible by using discrete-scale approach.

87 The previous paragraph explains why the coupling between conduction and radiation directly within the 3D
88 detailed geometries of the cellular ceramics is investigated [19, 28, 29]. These numerical advances are clearly
89 driven by the increasing access to X-ray tomography experiments for determining the precised topology of real-
90 world materials, and/or to the virtual generation of 3D realistic digitized images. For cellular ceramics, the
91 typical size of cells arranged within these porous materials (~ 0.5 – 2 mm) corresponds to the available spatial
92 resolution of laboratory-scale tomographic setups (~ 5 – 20 μm). This makes it easy to digitize real-world repre-
93 sentative elementary volumes of materials, and perform uncoupled conductive and radiative numerical analysis
94 on these volumes [23, 30]. However, when conjugate heat transfers are being investigated, the present-day nu-
95 merical approaches are limited to 3D images with modest volumes. This is due to important computational cost
96 required to reproduce the underlying heat transfers [18, 10]. Detailing and solving accurately discrete problems
97 on these complex geometries requires meshes with large number of elements.

98 In this study we solve and analyze the conduction–radiation coupling (under vacuum) within discrete-scale
99 ceramic samples operating at temperatures ranging from 1200 K to 1800 K. The finite element method is
100 used to solve the underlying partial differential equations of the conduction–radiation physics. We focus our
101 effort on SiC-based macroporous samples, this semiconducting material being intensively studied for designing
102 high-temperature systems [31, 8, 32, 29]. Our deterministic simulations are based on tightly coupled vectorial
103 FE for solving the radiation physics and Galerkin FE for solving the conduction physics. Our vectorial FE
104 solver [33, 34] was previously developed only for handling the radiation physics within participating media. In
105 this article, we extend its capabilities to solve conduction–radiation physics efficiently.

106 The rest of the paper is as follows. Section 2 details the model of coupled conduction and radiation physics
107 within cellular ceramics that are of interest to this study. Section 3 introduces the main numerical strategies,
108 the variational forms, the implemented algorithm, and the parallel domain decomposition strategy. With the
109 aim of understanding and characterizing conduction–radiation coupling within open-cell cellular ceramics, in
110 section 4, we perform extensive numerical experiments on topologically different cellular ceramic materials. A
111 detailed discussion on the behavior of these different porous ceramic samples is also included. The paper then
112 ends with concluding remarks in section 5.

113 2. Model of coupled conduction and radiation

114 For the global energy transfer within a SiC-based open-cell cellular ceramic at high temperature, both
 115 conduction and radiation take place consequently within its solid and void phases. On one hand, the opaque
 116 solid phase (SiC ligament network) is subjected to heat conduction driven by large temperature gradients
 117 and restricted radiative sources on its boundaries. On the other hand, the transparent void phase around and
 118 inbetween the solid SiC ligaments is subjected to radiation. The coupling process between the two phases occurs
 119 in the vicinity of their shared boundary. Opaque materials allow for implementing such coupling conditions as
 120 all radiation received by the borders of an opaque medium travels negligible distances within the volume before
 121 being absorbed. This certainly is the case for SiC ligaments (microstructures), the material considered in this
 122 article, as shown in [25].

123 Before further describing the mathematical model that governs the conduction–radiation physics within
 124 the open-cell ceramics, let us denote the open bounded set $\Omega_s \subset \mathbb{R}^3$ (resp. $\Omega_v \subset \mathbb{R}^3$) representing the solid
 125 (resp. void) phase domain. The solid (resp. void) phase boundary is denoted $\partial\Omega_s$ (resp. $\partial\Omega_v$). The solid–void
 126 interface is denoted $\Gamma = \partial\Omega_s \cap \partial\Omega_v$. Also, let \mathbf{n}_s (resp. \mathbf{n}_v) denote the outward unit vector normal to the solid
 127 (resp. void) phase.

128 In this article, the conduction physics within the open-cell ceramics is solved using the steady-state heat
 129 conduction equation (HCE), which we denote \mathcal{E}_{HCE} . The conduction problem then consists in searching for a
 130 scalar-valued function $T : \Omega_s \mapsto \mathbb{R}$ such that:

$$\mathcal{E}_{\text{HCE}} = -\nabla \cdot \lambda \nabla T = 0 \quad \forall \mathbf{x} \in \Omega_s \subset \mathbb{R}^3, \quad (1)$$

131 where T denotes the material temperature at spatial location $\mathbf{x} = (x, y, z)$ and λ denotes the homogeneous
 132 thermal conductivity of the material. Note that since the conduction–radiation coupling source term is restricted
 133 to the surfaces of the SiC ligament network, there is no source term in this equation.

134 We further use the steady-state discrete ordinates radiative transfer equations [35] for solving the radiation
 135 physics involved, by semi-discretizing the integro-differential radiative transfer equation. From here on, this
 136 semi-discretized radiative transfer equation set will be referenced as RTE. The radiative problem then consists
 137 in searching for N_d scalar-valued functions $\{I_m\}_{m=1}^{N_d} : \Omega_v \mapsto \mathbb{R}$ that satisfy a set of N_d coupled equations,

$$\mathcal{E}_{\text{RTE}} = \{s_m \cdot \nabla I_m = 0\}_{m=1}^{N_d} \quad \forall \mathbf{x} \in \Omega_v \subset \mathbb{R}^3, \quad (2)$$

138 where N_d is the total number of discrete directions (ordinates), I_m is the m th discrete radiative intensity, and
 139 \mathbf{s}_m is the m th discrete direction vector. One could refer to [36, 37] for detailed explanations on the radiative
 140 transfer equation (RTE), and to [38, 39] for the conditions applied on diverse boundaries. For the coupled
 141 conduction–radiation physics, we impose the following boundary conditions.

- 142 • A Dirichlet condition for \mathcal{E}_{HCE} is prescribed at both ends of the solid phase (the subscript ‘D’ stands for
 143 ‘Dirichlet’):

$$\begin{aligned} T &= T_{s,g-}^\partial \quad \text{on } \partial\Omega_{s,D,-} \subset \Gamma; \partial\Omega_{s,D,-} = \{\mathbf{x} \in \partial\Omega_s, \mathbf{x} < \delta + \min_{\Omega_s} \mathbf{x}'\}, \\ T &= T_{s,g+}^\partial \quad \text{on } \partial\Omega_{s,D,+} \subset \Gamma; \partial\Omega_{s,D,+} = \{\mathbf{x} \in \partial\Omega_s, \mathbf{x} < -\delta + \max_{\Omega_s} \mathbf{x}'\}. \end{aligned} \quad (3)$$

144 In this relationship, δ is a sufficiently small positive user-defined parameter so that the Dirichlet condition
 145 is applied on a boundary of sufficiently large enough area, i.e. $|\partial\Omega_{s,D,\pm}| > \epsilon$. $T_{s,g+}^\partial$ and $T_{s,g-}^\partial$ are the given
 146 hot and cold Dirichlet temperatures, respectively.

- 147 • \mathcal{E}_{HCE} is additionally supplied with the flux exchange (Neumann) condition, which takes into account the
 148 outgoing and the incoming radiation for the solid phase:

$$-\lambda \nabla T \cdot \mathbf{n}_s = \varepsilon \sum_{m=1}^{N_d} I_m w_m |\mathbf{s}_m \cdot \mathbf{n}_v| \mathbb{1}_{[\Gamma \cap \mathbf{s}_m \cdot \mathbf{n}_v > 0]} - \varepsilon \sigma n_v^2 (T_{s-v}^\partial)^4 \quad \text{on } \partial\Omega_s \setminus \partial\Omega_{s,D,\pm}. \quad (4)$$

149 In this equation, T_{s-v}^∂ represents the solid–void interface temperature, ε denotes the emissivity of the
 150 material, σ denotes the Stefan–Boltzmann’s constant, n_v is the refraction index of the solid–void interface,
 151 w_m is the quadrature weight such that $w_m = 4\pi/N_d$, and $\mathbb{1}$ denotes the Heaviside step function which
 152 results in zero or one depending on the considered Boolean operation, i.e., $\mathbb{1}_{[\Gamma \cap \mathbf{s}_m \cdot \mathbf{n}_v > 0]}$ equals to one
 153 if and only if $\Gamma \cap \mathbf{s}_m \cdot \mathbf{n}_v > 0$ and zero elsewhere. In this equation, the first term in the right-hand
 154 side denotes the incoming radiation flux (due to integration between the ligaments), and the second term
 155 denotes the emission loss.

- 156 • For the void phase in which \mathcal{E}_{RTE} is solved, the temperature on the boundary of the solid medium comes
 157 into play as the initial boundary condition (the subscript ‘in’ stands for ‘input’):

$$\{I_{m,\text{in}}\}_{m=1}^{N_d} = \frac{1}{\pi} \sigma \varepsilon n_v^2 (T_{s-v}^\partial)^4 \quad \text{on } \Gamma, \mathbf{s}_m \cdot \mathbf{n}_v < 0. \quad (5)$$

158 This type of boundary condition is often called a diffused boundary condition.

- 159 • The specular reflection boundary condition is also prescribed for \mathcal{E}_{RTE} (the subscript ‘R’ stands for
160 ‘reflective’):

$$\{I_{m,\text{R}}\}_{m=1}^{N_d} = \left\{ \rho \sum_{j=1}^{N_d} \delta_{m,j}(\mathbf{n}_v) I_j \mathbb{1}_{[\Gamma \cap \mathbf{s}_j \cdot \mathbf{n}_v > 0]} \right\}_{m=1}^{N_d} \quad \text{on } \Gamma, \quad (6)$$

161 where, ρ denotes the surface reflectivity, $\rho = (1 - \varepsilon)$, and $\delta_{m,j}$ denotes the partition ratio coefficient. For
162 details on $\delta_{m,j}$ see [40].

- 163 • The vacuum boundary condition is also applied to the void phase. All the six outer boundaries, which
164 form in fact the virtual bounding box of the ceramic, are considered radiatively cold. As such, radiation
165 can pass on to the surroundings.

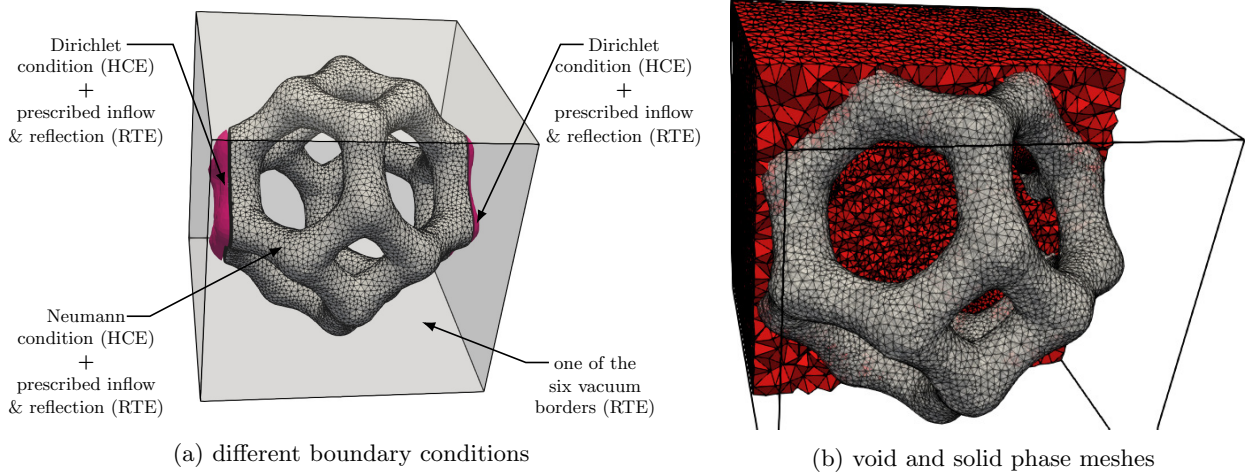


Figure 1: boundary conditions and meshes for a standalone Kelvin cell.

166 For a standalone Kelvin cell, the various boundaries on which these conditions act are presented in fig. 1a.

167 3. Finite elements model

168 The coupled conduction–radiation physics is governed by the steady-state heat equation (1) and the steady-
169 state discrete ordinates radiative transfer equation (2). Dirichlet boundary conditions eq. (3), along with flux
170 conditions eq. (4) are applied to the heat conduction problem. Eventually, the N_d inflow conditions eq. (5) are
171 applied to the radiation problem.

172 Before proceeding further, let us introduce Ω_s^h (resp. Ω_v^h) as the finite element mesh of the solid (resp. void)
173 phases, cf. fig. 1b. For the sake of visualization, we present a coarse solid mesh Ω_s^h (in gray) for a Kelvin cell
174 surrounded by a clipped void phase mesh Ω_v^h (in red). It should be noted that the two meshes are conforming at
175 the solid–void interface. This facilitates interpolation of different variables between both finite element spaces
176 defined on each mesh.

177 Finite element modeling is used to solve \mathcal{E}_{HCE} . The variational form of the heat conduction problem, $\mathcal{E}_{\text{HCE}}^h$,
178 consists in searching $T \in H_g^1(\Omega_s^h)$ such that:

$$\begin{aligned} \mathcal{E}_{\text{HCE}}^h = & \int_{\Omega_s^h} \lambda \nabla T \cdot \nabla v \, d\mathbf{x} - \int_{\partial\Omega_s^h} \left(\varepsilon \sum_{m=1}^{N_d} I_m w_m |\mathbf{s}_m \cdot \mathbf{n}_v| \mathbb{1}_{[\Gamma \cap \mathbf{s}_m \cdot \mathbf{n}_v > 0]} \right) v \, d\mathbf{x} \\ & + \int_{\partial\Omega_s^h} \left(\sigma \varepsilon n_s^2 T \left(\widehat{T}_{s-v}^\partial \right)^3 \right) v \, d\mathbf{x} = 0 \quad \forall v \in H^1(\Omega_s^h). \end{aligned} \quad (7)$$

179 Here, T_{s-v}^∂ is the interface temperature, $H_g^1(\Omega_s^h)$ is a subspace of $H^1(\Omega_s^h)$ with functions that satisfy Dirichlet
180 conditions eq. (3).

181 The heat conduction problem $\mathcal{E}_{\text{HCE}}^h$ has been linearized by including the third-order term $\left(\widehat{T}_{s-v}^\partial \right)^3$, with $\widehat{T}_{s-v}^\partial$
182 assumed to be a known quantity when solving $\mathcal{E}_{\text{HCE}}^h$. The second term in eq. (7) is the radiation gain, and the
183 final term is the emission loss.

184 Finite elements are also used to solve \mathcal{E}_{RTE} within the void phase. More precisely, using a vectorial finite
 185 element space, whose advantages over traditional spaces are pointed out in [33, 41], it is possible to precondition
 186 and solve the discretized equation efficiently [42].

187 To do so, let the vectorial radiative intensity \mathbb{I} gather the set of N_d unknown components of the radiative
 188 intensity in all prescribed discrete directions, such that $\mathbb{I} = (I_1, I_2, \dots, I_{N_d})$. In the same fashion, let the vector
 189 of directions $\mathbb{S} = (\mathbf{s}_1, \mathbf{s}_2, \dots, \mathbf{s}_{N_d})$. Further, let the vectorial test function \mathbb{V} be a vector of N_d test functions,
 190 such that $\mathbb{V} = (v_1, v_2, \dots, v_{N_d})$, with each v_m being defined in a Sobolev space $H^1(\Omega_v^h)$, so that the vectorial
 191 test function is in the vectorial finite element space $\mathbb{H}^1(\Omega_v^h) = H^1(\Omega_v^h) \times H^1(\Omega_v^h) \times \dots \times H^1(\Omega_v^h)$. With the use
 192 of vectorial finite elements, the resulting variational form is then a single equation, while the use of scalar finite
 193 element schemes results in N_d equations. The corresponding vectorial FE variational problem, $\mathcal{E}_{\text{RTE}}^h$, consists
 194 in searching $\mathbb{I} \in \mathbb{H}^1(\Omega_v^h)$ such that:

$$\begin{aligned} \mathcal{E}_{\text{RTE}}^h = & \int_{\Omega_v^h} (\mathbb{S} \cdot \nabla \mathbb{V})^\top (\gamma \mathbb{S} \cdot \nabla \mathbb{I} - \mathbb{I}) \, d\mathbf{x} + \int_{\Gamma^h} \left((\mathbb{R}_{\text{R}} : \mathbb{S} \cdot \mathbf{n}_v : \mathbb{I})^\top \mathbb{V} \right) \, d\mathbf{x} \\ & + \int_{\Gamma^h} \left(\frac{1}{\pi} \sigma \varepsilon n_v^2 \left(\hat{T}_{\text{s-v}}^\partial \right)^4 \left((\mathbb{S} \cdot \mathbf{n}_v : \mathbb{1}_{[\mathbb{S} \cdot \mathbf{n}_v < 0]})^\top \mathbb{V} \right) \right) \, d\mathbf{x} = 0 \quad \forall \mathbb{V} \in \mathbb{H}^1(\Omega_v^h). \end{aligned} \quad (8)$$

195 In this equation, $\gamma : \Omega_v^h \mapsto \mathbb{R}^+$ is the SUPG (Streamline Upwind Petrov–Galerkin) [43] stabilizing param-
 196 eter chosen according to recommendations provided in [44]. $\hat{T}_{\text{s-v}}^\partial$ is the known interface temperature. \mathbb{R}_{R}
 197 denotes the specular reflection operator (table) which is constructed from the knowledge of $\rho(n_v, n_s, \mathbf{n}_v, \mathbf{s}_m)$
 198 and $\delta(n_v, n_s, \mathbf{n}_v, \mathbf{s}_m)$ that denote the solid–void interface reflectivity and partition ratio coefficient, respectively.
 199 These are parameters based on the partition ratio method proposed in [40]. In eq. (8), we also introduced the
 200 following notations, $\mathbb{A}^\top \mathbb{B} = \sum_i \mathbb{A}_i \mathbb{B}_i$ and $(\mathbb{A} : \mathbb{B})_i = \mathbb{A}_i \mathbb{B}_i$, for the sake of conciseness.

201 The first integral of $\mathcal{E}_{\text{RTE}}^h$ deals with the transport of radiation within the bulk of the medium, the second
 202 integral deals with the physics of specular reflection on the shared solid–void interface, and the last integral
 203 (surface emission) is the influx boundary condition (diffused boundary condition).

204 The full steady-state problem gathering eqs. (7) and (8) is nonlinear. As such, in this study, starting from
 205 an initial guess, the two problems are solved successively one after the other, in a staggered fashion until the
 206 convergence is reached.

207 Algorithm 1 schematically presents the iterative algorithm to solve the conduction–radiation physics within
 208 the SiC structures. Lines 1 to 3 represent the initial setup phase of our algorithm which is done once. For the
 209 nonlinear solver (lines 4 to 13), a L_∞ norm test is used in terms of the change in the solution between iterates,
 210 with a tolerance $\epsilon = 10^{-2}$. Similar stopping criteria for the nonlinear iterations have also been suggested
 211 in [45, 38].

Input: geometries Ω_s and Ω_v , physical parameters: $\lambda, \varepsilon, n_v, \dots$, and numerical parameters: $\epsilon, \gamma, N_d, \delta, \dots$

- 1 Build the interpolation operator $\mathcal{P}_s^\vee : \partial\Omega_s \mapsto \partial\Omega_v$ such that $T(\mathbf{x} \in \partial\Omega_v) = \mathcal{P}_s^\vee T(\mathbf{x} \in \partial\Omega_s)$
- 2 Build the reverse interpolation operator $\mathcal{P}_v^\delta : \partial\Omega_v \mapsto \partial\Omega_s$
- 3 Initialize $\{I_m\}_{m=1}^{N_d}$ and $\hat{T}_{\text{s-v}}^\partial$ to zero
- 4 **repeat**
- 5 Solve \mathcal{E}_{HCE} with given boundary conditions eqs. (3) and (4) $\rightsquigarrow T(\mathbf{x} \in \Omega_s)$
- 6 Extract the solution on the boundary $T_s^\partial = T(\mathbf{x} \in \Gamma)$
- 7 **if** $\|T_s^\partial - \hat{T}_{\text{s-v}}^\partial\|_\infty < \epsilon$ **then return** $T(\mathbf{x} \in \Omega_s), \{I_m(\mathbf{x} \in \Omega_v)\}_{m=1}^{N_d}$
- 8 Update the solution on the boundary $\hat{T}_{\text{s-v}}^\partial = T_s^\partial$
- 9 Interpolate on the boundary with $T_v^\partial = \mathcal{P}_s^\vee T_s^\partial$
- 10 Solve \mathcal{E}_{RTE} with given boundary conditions eqs. (5) and (6) $\rightsquigarrow \{I_m(\mathbf{x} \in \Omega_v)\}_{m=1}^{N_d}$
- 11 Extract the radiative flux $\phi_v^\partial(\mathbf{x} \in \Gamma) = \varepsilon \sum_{m=1}^{N_d} I_m w_m |\mathbf{s}_m \cdot \mathbf{n}_v| \mathbb{1}_{[\Gamma \cap \mathbf{s}_m \cdot \mathbf{n}_v > 0]}$
- 12 Interpolate on the boundary with $\phi_v^\partial = \mathcal{P}_v^\delta \phi_v^\partial$
- 13 **until convergence**

Algorithm 1: iterative algorithm for the coupled conduction–radiation modeling.

212 At this stage, the finite element formulations to solve the coupled conduction–radiation physics involve a
 213 scalar finite element problem eq. (7) (HCE) and a vectorial finite element problem eq. (8) (RTE). Overall, the
 214 coupled finite element model requires the solution of a problem with $N_d + 1$ fields. A high value of N_d is needed
 215 if the geometry is complex and if the RTE is to be solved with high accuracy [25]. In this study, we have used
 216 $N_d = 512$ (second octahedral refinement), as such, the coupled finite element problem of conduction–radiation
 217 requires to solve a 513 field problem, with each field being defined at all spatial nodes.

218 To do so in a distributed-memory parallelism context, the global mesh (void or solid) Ω^h is partitioned into
 219 N_p non-overlapping meshes $\{\Omega_i^h\}_{i=1}^{N_p}$ (subdomains) using ParMETIS [46]. A subdomain is then assigned to
 220 a single MPI process, and the global matrices for the RTE and the HCE may be assembled in a distributed

221 fashion using eqs. (7) and (8), respectively. The open-source finite element kernel FreeFEM [47] is used for the
 222 local matrix assemblies. The open-source library PETSc [48] is used for the parallel matrix assemblies and for
 223 solving the linear systems.

224 4. Numerical experiments

225 In this section, we detail and discuss the results of discrete-scale numerical experiments performed on different
 226 SiC-based open-cell cellular ceramic structures and on the related standalone SiC cells. To study the pore-level
 227 characteristics of conduction–radiation coupling in tests 1A to 1D, we analyze the standalone cubic and Kelvin
 228 cells at 80% and 90% porosity each. Structurally, the cubic cells are 0.5 cm in length, and the Kelvin cells
 229 are 0.5 cm in diameter. These cells are constructed with ligaments that are ~ 0.1 cm in diameter for the 80%
 230 porosity structures and ~ 0.069 cm for the 90% porosity structures. To study the full-scale open-cell cellular
 231 ceramic structures, in tests 2A to 2F, we analyze the cubic, Kelvin, and pseudo-random structures at 80%
 232 and 90% porosity each. At this level, let us precise that the term “pseudo-random” means that the position
 233 in space of a cell is not totally random but affected by the spatial arrangement of the neighboring cells. For
 234 simplicity, we now only use the term random instead of pseudo-random. Structurally, the cubic- and Kelvin-cell
 235 ceramic samples are constructed by joining together 125 standalone cubic and Kelvin cells, i.e., 5 cells per spatial
 236 directions, $5 \times 5 \times 5 = 125$. Thus, cubic- and Kelvin-cell ceramic samples (tests 2A, 2B, 2C, and 2D) at length
 237 2.5 cm are 5 times larger. The random-cell ceramic samples use the same length of 2.5 cm. The ligaments of
 238 all of these geometries (the standalone cells or the full-scale ceramics) are assumed to be made out of highly
 239 dense 6H-SiC sintered ceramic. For this material, we assume $\varepsilon = 0.9$ and $\lambda = 0.3 \text{ W cm}^{-1} \text{ K}^{-1}$. This λ is in fact
 240 an average thermal conductivity constructed from the high-temperature experimental data for monocrystalline
 241 6H-SiC, given in [49]. Overall, the description of all our tests is provided in table 1.

Test	Type	Cell	ϕ	S_v	k	unknowns _{HCE}	unknowns _{RTE}
1A	standalone	cubic	80	7.14	4	29,985	23,064,576
1B	standalone	cubic	90	5.39	5	18,248	25,138,176
1C	standalone	Kelvin	80	8.46	7	33,549	26,625,024
1D	standalone	Kelvin	90	5.91	9	20,629	29,829,632
2A	full-scale	cubic	80	4.44	6	267,544	231,302,656
2B	full-scale	cubic	90	3.51	7	201,787	263,202,304
2C	full-scale	Kelvin	80	6.77	8	388,020	338,101,760
2D	full-scale	Kelvin	90	5.24	9	374,928	517,838,848
2E	full-scale	random	80	4.94	7	587,203	389,615,616
2F	full-scale	random	90	4.13	10	449,117	414,130,176

Table 1: characteristics of the standalone SiC cell and the full-scale SiC ceramic numerical tests. For the mentioned properties read ϕ in %, S_v in cm^{-1} , k is total number of nonlinear iterations for solving the coupled conduction–radiation problem.

242 All the tests (1A to 1D and 2A to 2F) were performed twice, once with the standalone conduction physics
 243 and once with the coupled conduction–radiation physics. For the standalone conduction simulations, \mathcal{E}_{HCE} was
 244 solved by using Dirichlet boundary conditions $T_{s,g+}^{\partial} = 1800 \text{ K}$ and $T_{s,g-}^{\partial} = 1200 \text{ K}$, on the hot and cold borders,
 245 respectively, see eq. (3), and with a null exchange flux everywhere else. For the coupled conduction–radiation
 246 simulations, \mathcal{E}_{HCE} and \mathcal{E}_{RTE} are solved in a coupled way according to the procedure explained in section 3.
 247 For the boundary conditions, the same Dirichlet conditions are used, plus Neumann conditions from eq. (4) for
 248 \mathcal{E}_{HCE} . For \mathcal{E}_{RTE} , the boundary conditions given in eqs. (5) and (6) are applied. Next, as a numerical choice in
 249 the discretization of the RTE, the number of discrete ordinates, N_d , has been chosen equal to 512.

250 To analyze the behavior of the upcoming numerical experiments, we introduce the following quantities.

- Radiative heat flux on the solid–void interface:

$$Q_r^+(\mathbf{x} \in \Gamma^h) = \sum_{m=1}^{N_d} I_m(\mathbf{x}) w_m |\mathbf{s}_m \cdot \mathbf{n}_v(\mathbf{x})| \mathbb{1}_{[\Gamma^h \cap \mathbf{s}_m \cdot \mathbf{n}_v > 0]}.$$

251 Here, w_m is the quadrature weight such that $w_m = 4\pi/N_d$. $Q_r^+(\mathbf{x} \in \Gamma^h)$ defines the net amount of radiative
 252 heat flux entering the solid interface along the direction of its normal vector $\mathbf{n}_s = -\mathbf{n}_v$. $Q_r^+(\mathbf{x} \in \Gamma^h)$ can
 253 be used as a metric for the absorbing quality of a structure.

- Total absorbed radiation on the ligament surface:

$$q_{\Gamma^h} = \int_{\Gamma^h} Q_r^+(\mathbf{x}) \, d\mathbf{x}.$$

254 This quantity measures the overall power of the sample to absorb incoming radiation.

- Radiative density in the void phase:

$$G(\mathbf{x} \in \Omega_v^h) = \sum_{m=1}^{N_d} I_m(\mathbf{x}) w_m.$$

255 Here, $G(\mathbf{x} \in \Omega_v)$ defines the total radiative energy (photon concentration) at a given point \mathbf{x} in Ω_v^h .

- z -averaged temperature \bar{T}_z , i.e, mean temperature for a given xy -plane located at $z = \hat{z}$:

$$\bar{T}_z(\mathbf{x} \in \Omega_s^h, z = \hat{z}) = \frac{\int_{\Omega_s^h} T(\mathbf{x}) \mathbb{1}_{[z=\hat{z}]} d\mathbf{x}}{\int_{\Omega_s^h} \mathbb{1}_{[z=\hat{z}]} d\mathbf{x}}.$$

256 This quantity is the plane-averaged scalar temperature that is often used in the cellular ceramics literature
257 to assess the thermal behavior of porous media.

- Volumetric surface of the structure:

$$S_v = \frac{\int_{\Gamma^h} d\mathbf{x}}{\int_{\Omega_s^h} d\mathbf{x} + \int_{\Omega_v^h} d\mathbf{x}}.$$

258 This quantity measures the surface area of ligaments per unit of volume. S_v is often directly linked to
259 volume-averaged properties of porous materials, like the effective extinction coefficient β_{eff} or the effective
260 thermal conductivity λ_{eff} , cf. [50].

261 4.1. Setup

262 *Topology generation.* The primary challenge in discrete-scale simulations of open-cell cellular ceramic ma-
263 terials is detailing their complex topologies. To tackle the problem of topology generation for these ceramics,
264 which is inherent of deterministic methods like the FEM, we have used an in-house virtual material genera-
265 tor genMat¹ [32]. Based on the marching cubes [51], genMat is able to generate topologies of various porous
266 materials with standalone cells and open-cell cellular ceramics.

267 The topologies of the standalone SiC cells used in tests 1A to 1D and the topologies of the full-scale SiC-based
268 ceramics used in tests 2A to 2F are presented in fig. 2 and fig. 3 respectively. As mentioned, the standalone
269 cells are 0.5 cm in size, while the full-scale ceramic samples are 2.5 cm.

270 *Meshing.* The voxel-based surface meshes from genMat contain millions of surface nodes, as is the case for
271 most X-ray micro-tomography surface meshes. Being voxel-based, these meshes are well suited for ray-tracing
272 algorithms based on random walks. However, constructing Delaunay meshes from these surface meshes was
273 not possible due to memory constraints. To deal with this problem, topology reconstruction through mesh
274 adaption based on a tuned Hausdorff metric [52] was used. This operation is performed by the open-source
275 library Mmg [53]. Finally, using the re-meshed surface topologies, the volumetric meshing is performed by
276 another open-source package, Gmsh [54]. This involves creating two tetrahedral meshes for both the solid
277 and the void phases. Additional details on the topology and the mesh generations are given in [55]. To
278 motivate reproducibility of our results, the standalone ceramic cell meshes, among other data, are provided as
279 supplementary resources to this paper.

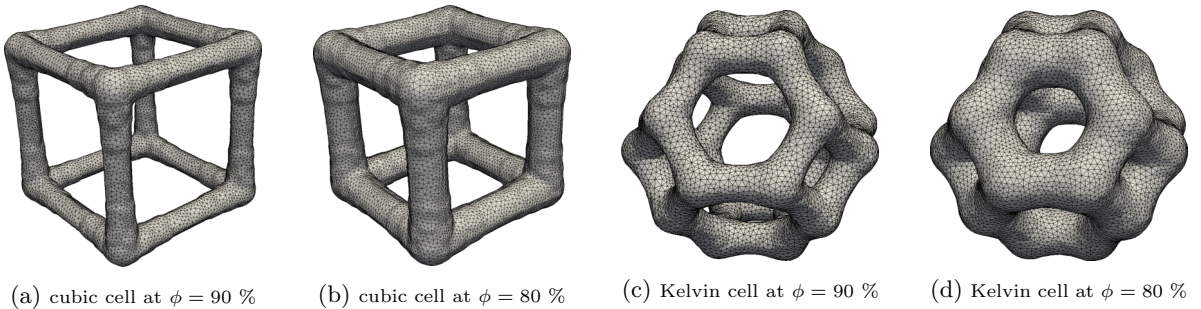


Figure 2: standalone cell topologies.

280 *Solver specifications.* For solving \mathcal{E}_{RTE} , the Jacobi-preconditioned BiCGSTAB method is used, with a
281 convergence tolerance on the relative residual set to 10^{-6} . As specified earlier, in all test cases, $N_d = 512$
282 discrete directions are used. The number of unknowns for the RTE linear systems is given in the last column
283 of table 1. For solving \mathcal{E}_{HCE} , an exact LU factorization is computed by MUMPS [56] (interfaced with PETSc).

¹genMat: a C++ and Qt based software developed collaboratively by LTeN & IUSTI, CNRS laboratories, France.

284 More advanced preconditioners could have been used, like multigrid methods, but the number of unknowns for
 285 this field, reported in the 7th column of table 1, is rather small. For all test cases, only few nonlinear iterations
 286 are needed to reach convergence, as can be seen from the 6th column of table 1.

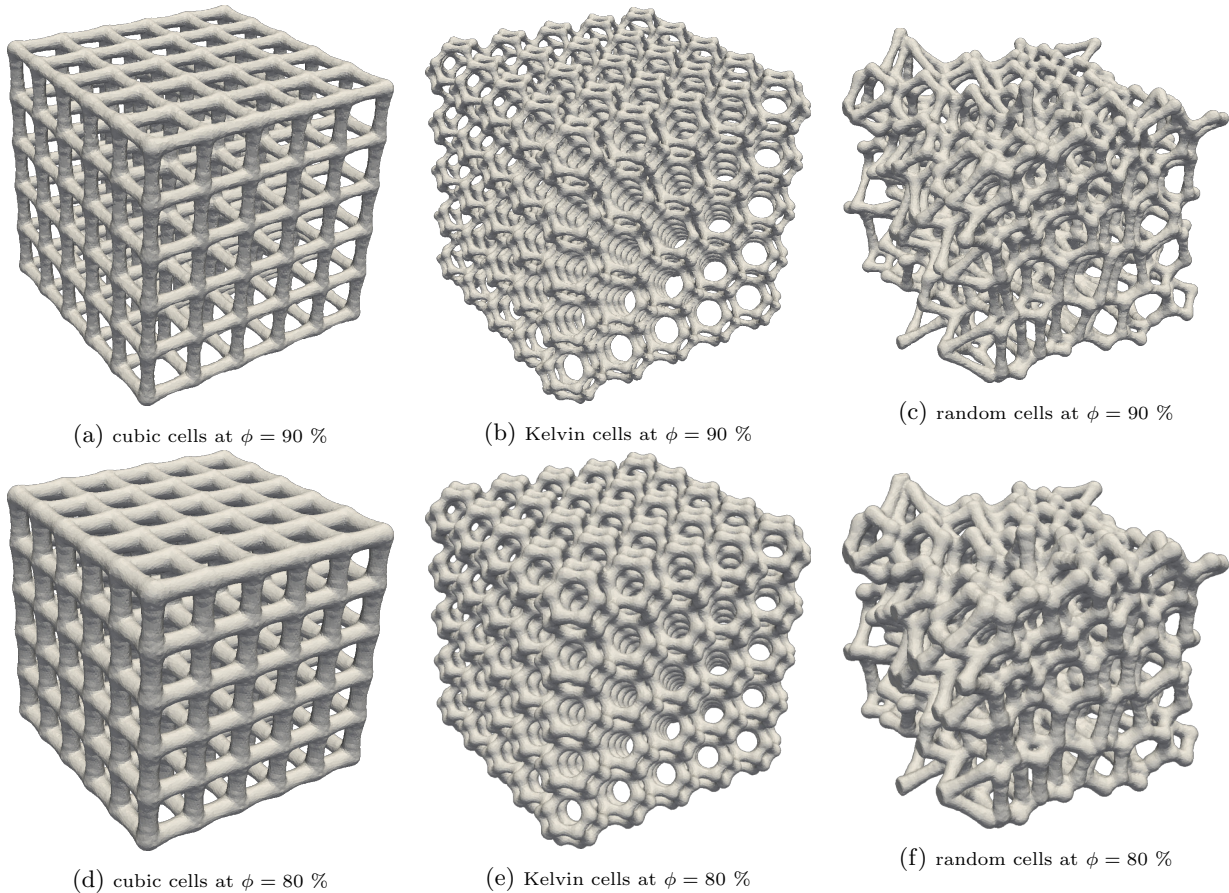


Figure 3: full-scale ceramic topologies.

287 LIGER, a cluster hosted at ICI, Centrale Nantes, France, was used to perform the numerical simulations.
 288 100 MPI processes were used to solve the standalone cell simulations (tests 1A to 1D) and 1,000 MPI processes
 289 were used to solve the full-scale ceramic simulations (tests 2A to 2F). These problems are solved in few minutes
 290 for each case.

291 The largest simulation of this study (90 % porosity Kelvin-cell ceramic structure) consists in solving a system
 292 of 0.52 billion unknowns for the radiation coupled to a system of 0.37 million unknowns for the conduction.
 293 For this test case, it took 9 iterations for the nonlinear solver to converge. This emphasizes the role of efficient
 294 solution techniques for discrete-scale conduction–radiation simulations.

295 Note that our radiation solver has been validated thoroughly using the method of manufactured solutions [33,
 296 34], and against other deterministic or Monte-Carlo benchmark results [41]. In particular, we verified that our
 297 solver is able to produce accurate radiative heat fluxes on surfaces. Besides these validation tests, in [41], we
 298 verified our conduction–radiation solver against experimental results provided in [14]. For this test, thermograms
 299 from the laser flash method applied to different metallic open-cell foams were analyzed and compared up to
 300 $T = 673$ K. We showed that our solver predict well the experimental temperatures with relative errors between
 301 2 % and 5 %.

302 4.2. Results and discussions

303 The coupled conduction–radiation temperature fields for the 90 % porosity SiC cubic- and Kelvin-cell samples
 304 are presented in fig. 4a. Based on the location from the hot Dirichlet boundary $\partial\Omega_{s,g+}^h$, the temperature within
 305 the cell ligaments quasi-linearly decreases from 1800 K to 1200 K. To investigate the heat flow characteristics,
 306 in fig. 4b, we present a heatline visualization from the coupled conduction–radiation simulations of the 90 %
 307 porosity standalone cubic- and Kelvin-cell structures (tests 1B and 1D). This represents the net heat flow as
 308 it passes through the SiC ligaments. A heatline is similar to a streamline, except that it visualizes the net
 309 energy flow caused due to heat transfer situations, c.f. [57, 58]. Heatlines, here, are constructed by numerical
 310 integration (performed in ParaView [59]) of the heat flux vector $(-\lambda dT/dx, -\lambda dT/dy, -\lambda dT/dz)^\top$. Heat
 311 energy flows through four distinct, but symmetric due to geometry, paths via the four central ligaments of the

312 cubic cell. For the Kelvin cell, due to its topology, a heatline bifurcation happens in the central region. Heatlines
 313 for the 80 % porosity standalone cell structures (tests 1A and 1C not shown here) had similar characteristics.

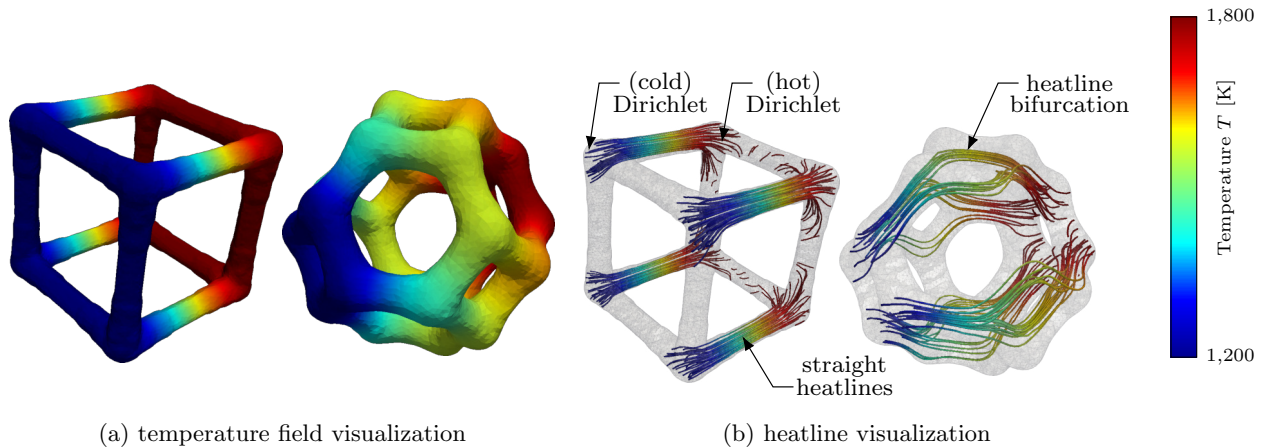


Figure 4: coupled conduction–radiation simulation results for the standalone SiC cubic and Kelvin cells at 90 % porosity.

314 Visualization of the radiative heat flux fields $Q_r^+(\mathbf{x} \in \Gamma^h)$ for the 90 % porosity standalone SiC cells is
 315 presented in fig. 5. For the cubic cell in fig. 5a, the inner corners of the cells near the hot border receive the
 316 maximum radiative heat flux, $\max(Q_r^+(\mathbf{x} \in \Gamma^h)) = 1.69 \text{ W cm}^{-2}$. We can observe how the inner faces of the SiC
 317 cubic-cell ligaments receive the higher amount of radiation, while the outer parts remain comparatively cold.
 318 The high radiative heat fluxes on the inner faces of the ligaments are due to the radiation energy interaction
 319 inbetween the ligaments. Indeed, due to the high-temperature radiation, energy is emitted by a ligament in
 320 different directions. Depending on its path, it either encounters a neighboring ligament (radiation interaction) or
 321 escapes directly to the surrounding via one of the six vacuum boundaries. Concerning the radiation interaction,
 322 a part of the energy, proportional to ε , gets absorbed by the ligament while the other part is reflected to
 323 other directions. A similar scenario exists for the SiC Kelvin cell, see fig. 5b. However, for this case, the
 324 maximum radiative heat flux $\max(Q_r^+(\mathbf{x} \in \Gamma^h)) = 2 \text{ W cm}^{-2}$ is higher than for the SiC cubic cell. Similar
 325 results were observed for the 80 % porosity SiC cubic- and Kelvin-cell structures. The Kelvin cell has a higher
 326 $\max(Q_r^+(\mathbf{x} \in \Gamma^h))$ than the cubic cell. It was also observed that more radiative heat flux is injected into the
 327 Kelvin cell than into the cubic cell. The SiC Kelvin cell has a more absorbing structure than the SiC cubic
 328 cell. From the Kirchhoff's principle, the Kelvin cell has a more emitting structure than the cubic cell. By this
 329 discussion, one could also say that, at a particular porosity (90 % or 80 %), the radiation plays a more prominent
 330 role in the SiC Kelvin-cell structures than in the SiC cubic-cell structures. Overall, the SiC Kelvin-cell structure
 331 maximizes the radiation gains compared to the SiC cubic-cell structure.

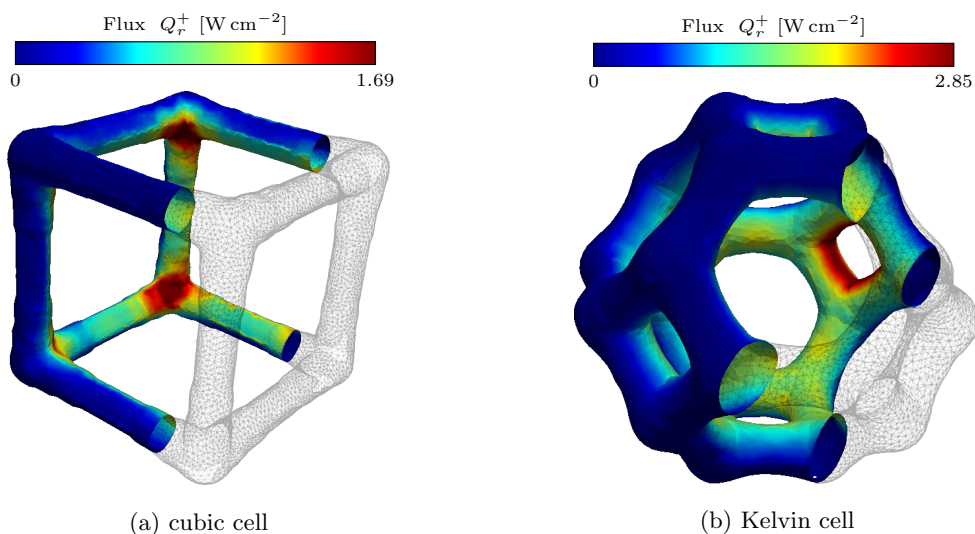


Figure 5: radiative heat flux on clipped surfaces of 90 % porosity standalone SiC cells.

332 Radiation densities $G(\mathbf{x} \in \Omega_v^h)$ for 90 % porosity standalone SiC cubic and Kelvin cells are displayed in fig. 6.
 333 It clearly shows that the radiation energy diffusion is greater in the SiC Kelvin cell than in the SiC cubic cell.
 334 First, the Kelvin cell has a higher value of S_v , see table 1. As a result, more energy is being emitted to the void

335 region leading to more radiation interaction between the ligaments. Second, the Kelvin cell has a greater surface,
 336 so there is more possibility for photons to be reflected and propagated further in the void region and ultimately
 337 interact with other ligaments. Eventually, the inner void region of the cubic cell has a greater volume. Thus,
 338 the greater area for effective radiation within the Kelvin cell increases the probability of interaction between
 339 the ligaments. Consequently, we observe the absorbing power q_{Γ^h} of the 90 % (resp. 80 %) porosity standalone
 340 SiC Kelvin cell is 2.4 (resp. 1.4) times higher than that of the cubic cell, see table 2. These results complement
 341 the conclusion from the last paragraph that the standalone SiC Kelvin cell maximizes radiation gains compared
 342 to the standalone SiC cubic cell.

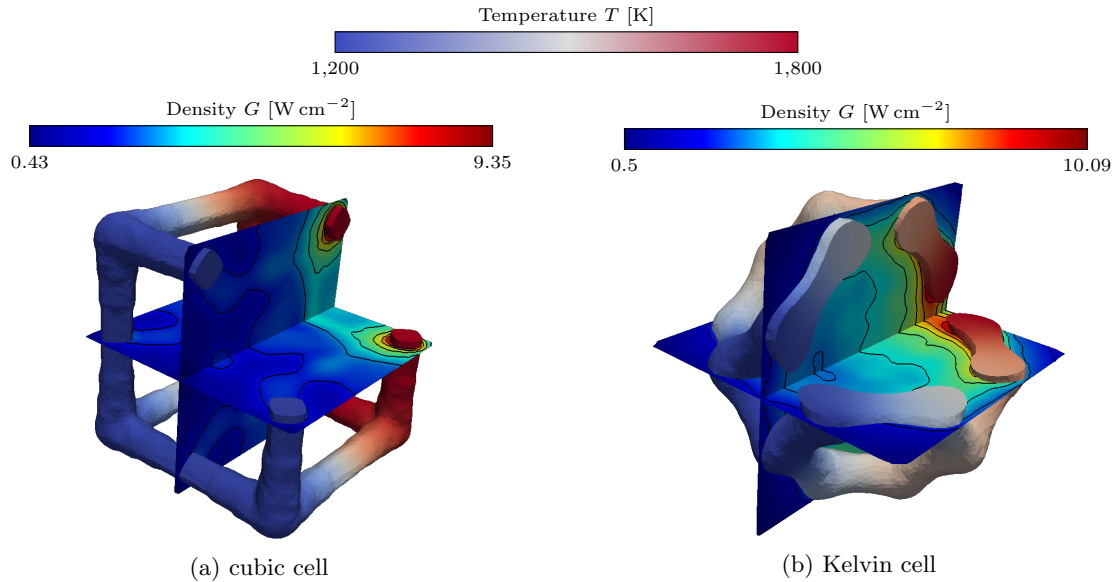


Figure 6: combined solution field visualization for the 90 % porosity standalone SiC cells: temperature field visualized for the solid part and radiative density field visualized for the orthogonal void cross-sections.

343 An analysis of conduction–radiation coupling effects within SiC cells is given in fig. 7 using \bar{T}_z . In these
 344 plots, dotted lines represent data acquired from conduction simulations while solid lines represent data from
 345 coupled conduction–radiation simulations. \bar{T}_z increases almost linearly from 1200 K to 1800 K in both Kelvin
 346 and cubic cells. The different profiles of \bar{T}_z for both cell is the direct effect of their ligament arrangements.
 347 The value of \bar{T}_z , for all ordinates z , is higher for the conduction–radiation than for the conduction only (except
 348 where the Dirichlet boundary conditions are imposed). This is a direct implication of the addition of radiation
 349 energy due to coupling.

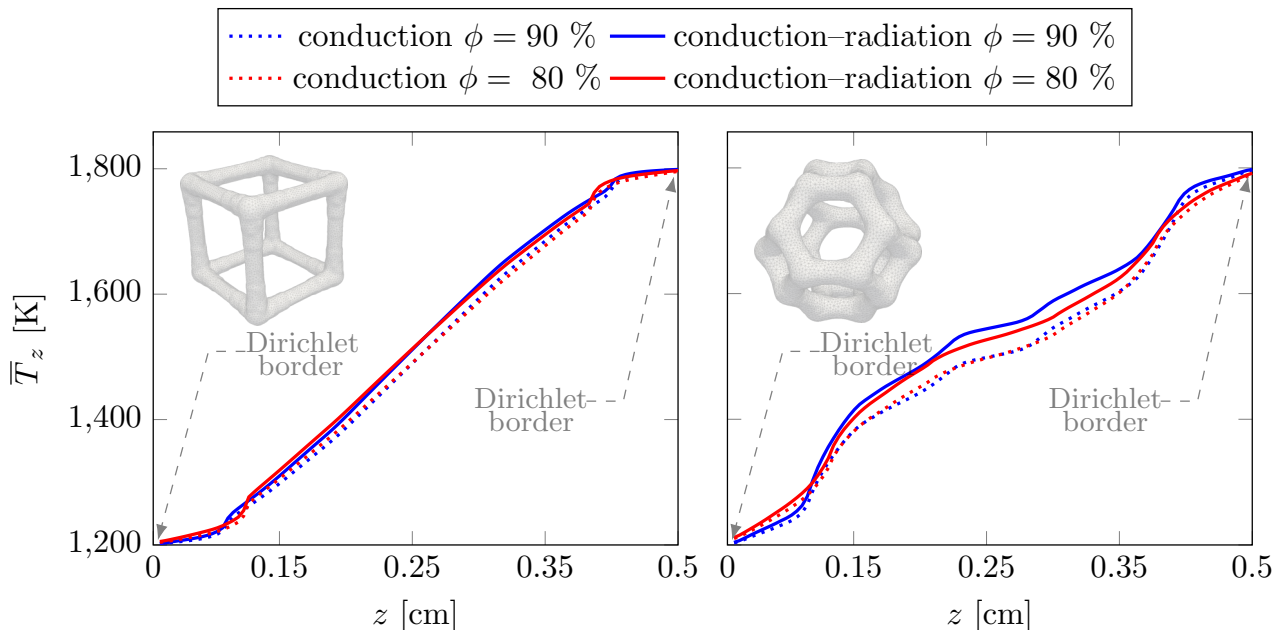


Figure 7: \bar{T}_z for conduction and conduction–radiation simulations for the standalone SiC cubic (left) and Kelvin (right) cells.

350 To quantify the effect of the coupling, we also plot the difference in \bar{T}_z , denoted $\Delta\bar{T}_z$, in fig. 8. The plots
 351 show that:

- 352 • \bar{T}_z for all topologies is under-predicted if radiation is not considered. This suggests a tight coupling of
 353 conduction and radiation, at least for the 80 % and 90 % porosities and for the used temperature range;
- 354 • \bar{T}_z varies the most in the central region of cells ($\Delta\bar{T}_z$ has a parabolic profile). This variation is greater
 355 in the Kelvin cell than in the cubic cell. Particularly, the 90 % (resp. 80 %) porosity Kelvin cell has a
 356 maximum increase of \bar{T}_z of 46 K (resp. 30 K);
- 357 • both 80 % and 90 % porosity cubic-cell simulations performed with conduction–radiation physics led to a
 358 parabolic-like increase in \bar{T}_z over the conduction alone physics. However, the porosity change did not show
 359 any effect in the magnitude of \bar{T}_z . A maximum variation of $\sim \pm 2$ K was observed. This insensitivity of the
 360 standalone SiC cubic-cell to porosity change (from 80 % to 90 %) suggests that the porosity change within
 361 such structures does not allow an increase in conduction–radiation transfer. Contrarily, the conduction–
 362 radiation behavior within standalone SiC Kelvin-cells is sensitive to porosity change (from 80 % to 90 %).
 363 A 44 % relative increase in $\max(\Delta\bar{T}_z)$ was observed for the 90 % porosity standalone Kelvin-cell compared
 364 to the 80 % porosity standalone Kelvin-cell.

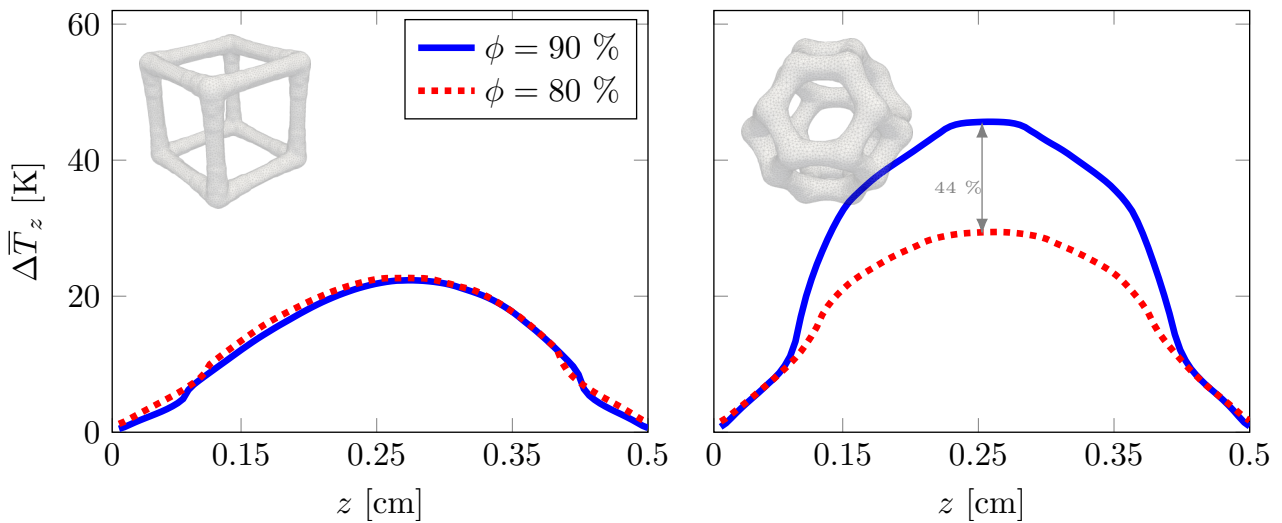


Figure 8: $\Delta\bar{T}_z$ for the standalone SiC cubic (left) and Kelvin (right) cells.

365 In fig. 9, we display the temperatures on the ligament networks of the full-scale SiC ceramics at 90 % porosity.
 366 These temperatures were obtained from conduction–radiation simulations (tests 2B, 2D, and 2F). Based on the
 367 location from the hot Dirichlet boundary, the temperature quasi-linearly decreases from 1800 K to 1200 K.

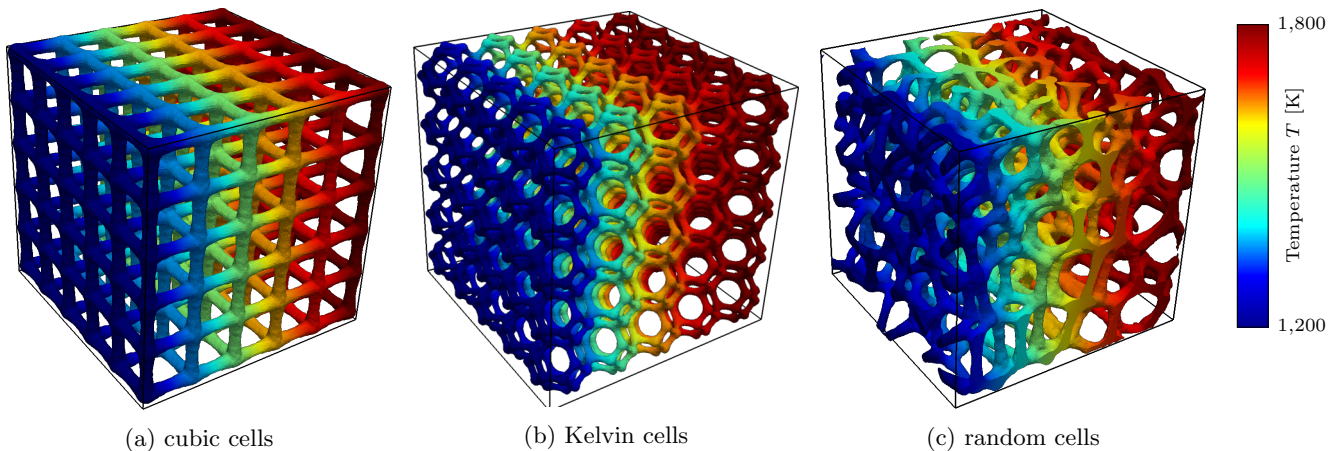


Figure 9: temperature fields for the 90 % porosity full-scale ceramic samples.

368 In fig. 10, heatlines for the 90 % full-scale ceramic samples are presented. Like for the standalone cells in
 369 fig. 4a, the heat flows from high to low temperatures imposed by the Dirichlet boundary conditions. Heatlines

are also used in fig. 11 to highlight the effect of conduction–radiation coupling or the lack thereof on heat transport. We used a truncated section of the 90 % porosity random-cell ceramic sample. Unlike in fig. 10, where heatlines originated from uniformly distributed point sources on a line, heatlines in fig. 11 originate from a single point source located at $(0.5, 0.5, 2.5)$. The fig. 11 highlights two key aspects of the coupled conduction–radiation heat transport: heat flows through different paths and heat energy propagates further. Similar results were observed for the 80 % porosity random-cell ceramic sample.

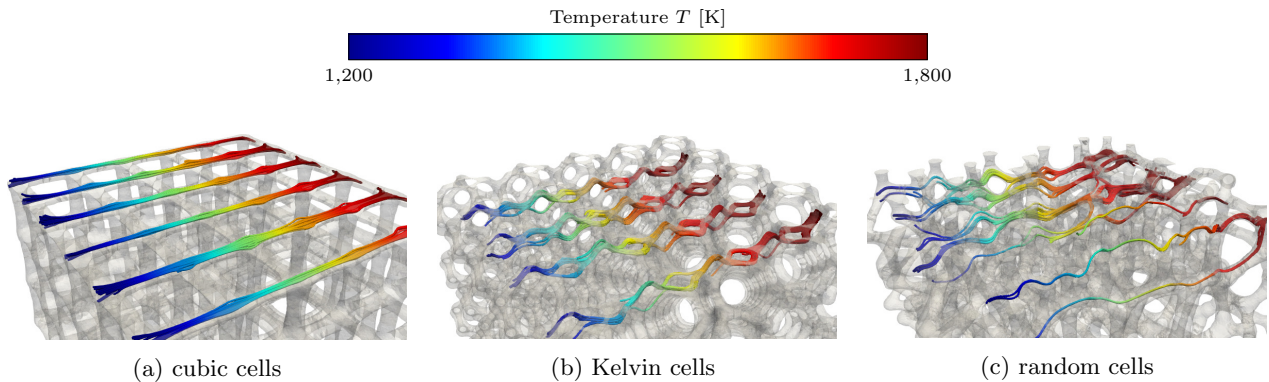


Figure 10: coupled conduction–radiation heatlines arising from a line source on the hot Dirichlet boundary for 90 % porosity ceramic samples.

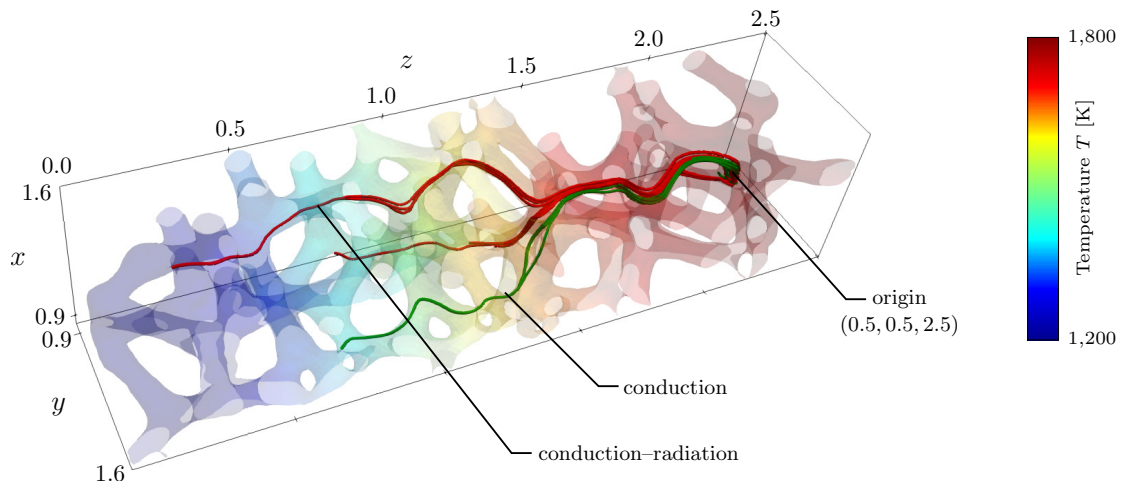


Figure 11: conduction (green) and conduction–radiation (red) heatlines from a point source on the hot Dirichlet boundary for the SiC random-cell ceramic sample at 90 % porosity.

Figures 12 to 14 display truncated views of the net radiative heat fluxes $Q_r^+(\mathbf{x} \in \Gamma^h)$ on the surfaces of the 90 % porosity SiC cubic-, Kelvin-, and random-cell ceramic structures. Among the deterministic ceramic structures, i.e., with cubic and Kelvin cells, the latter has the highest $\max(Q_r^+(\mathbf{x} \in \Gamma^h)) = 0.29 \text{ W cm}^{-2}$. Like for standalone SiC cells, higher values of $Q_r^+(\mathbf{x} \in \Gamma^h)$ are observed in the vicinity of the hot Dirichlet boundary and they decrease as one moves away from this boundary.

	standalone SiC cells				full-scale SiC cellular ceramics					
	cubic cells		Kelvin cells		cubic cells		Kelvin cells		random cells	
	80 %	90 %	80 %	90 %	80 %	90 %	80 %	90 %	80 %	90 %
$L_{\max(\Delta\bar{T}_z)}$	0.25	0.25	0.25	0.25	1.03	1.07	1.06	1.15	1.11	1.13
$\max(\Delta\bar{T}_z)$	21.97	22.58	27.40	41.63	41.70	64.52	74.35	140.54	50.48	92.00
q_{Γ^h}	0.37	0.41	0.52	0.99	2.87	3.98	5.29	7.57	4.09	5.03
β_{eff}	-	-	-	-	-	-	3.13	1.78	1.92	0.96

Table 2: maximum change $\max(\Delta\bar{T}_z)$ in K, distance of $\max(\Delta\bar{T}_z)$ to the hot boundary $L_{\max(\Delta\bar{T}_z)}$ in cm, effective extinction coefficient β_{eff} in cm^{-1} , and total radiation energy absorbed q_{Γ} in W, for the standalone cells and the full-scale ceramic structures.

In the same figures (figs. 12 to 14), we also present the radiative density profiles on two orthogonal void planes. Among the deterministic ceramic structures, the density distribution reaches its maximum in the

383 central regions, while it decreases towards the lateral faces. This lateral decrease in the radiative energy was
 384 not observed in the random-cell ceramic samples.

385 In table 1 values of the volumetric surface S_v for the cubic-, Kelvin-, and random-cell ceramic samples are
 386 provided. These values suggest that among the three different ceramic topologies examined, the Kelvin-cell
 387 topology has a greater surface area to emit/absorb radiation. Compared to the 90 % (resp. 80 %) porosity
 388 cubic-cell ceramic, the S_v of the Kelvin-cell ceramic is 1.49 (resp. 1.52) times larger. Similarly, in comparison to
 389 the 90 % (resp. 80 %) porosity random-cell ceramic, the S_v of the Kelvin-cell ceramic is 1.26 (resp. 1.37) times
 390 larger. As a consequence, in table 2 we observe higher values of q_{Γ^h} for the Kelvin-cell ceramic samples, in
 391 comparison to the cubic-cell or random-cell samples, suggesting higher absorbing capabilities of the Kelvin-cell
 392 ceramic samples. Precisely, the value of q_{Γ^h} for the 90 % porosity Kelvin-cell ceramic sample is 1.9 (resp. 1.5)
 393 times more than that of the 90 % porosity cubic-cell (resp. random-cell) ceramic sample. At 80 % porosity,
 394 the value of q_{Γ^h} for the Kelvin-cell ceramic sample is 1.8 (resp. 1.3) times more than that of the cubic-cell
 395 (resp. random-cell) ceramic sample.

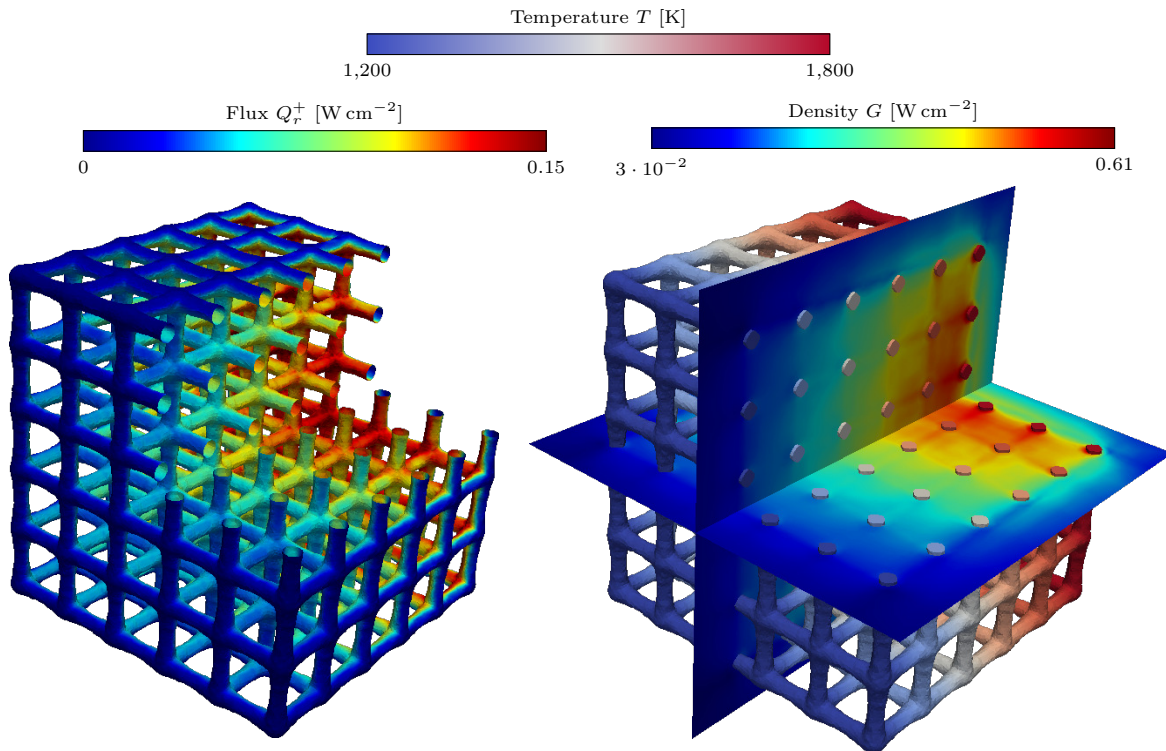


Figure 12: combined solution field visualization for the SiC cubic-cell ceramic sample at 90 % porosity. Right: temperature field visualized for the solid part and radiative density field visualized for the orthogonal void cross-sections. Left: radiative heat flux field visualized for the truncate solid phase boundary.

396 As for the standalone SiC cells, an analysis of conduction–radiation coupling effects within different ceramic
 397 samples is given in fig. 15 using \bar{T}_z . From these plots, observe that a porosity change from 90 % to 80 % has no
 398 effect when only conduction is considered. For the coupled conduction–radiation simulations, a porosity change
 399 from 90 % to 80 % has a clear effect on \bar{T}_z . As expected, due to higher probabilities of interactions of radiation
 400 between ligaments, \bar{T}_z is higher in the central region of the ceramics for the coupled simulations.

401 To quantify the effect of the coupling, we also plot the difference in \bar{T}_z , denoted $\Delta\bar{T}_z$, in fig. 16. The plots
 402 show that:

- 403 • $\Delta\bar{T}_z$ for the 90 % porosity ceramic samples is overall higher than for the 80 % porosity ceramic samples.
 404 A similar qualitative observation could be derived from analyzing the volumetric surface data S_v provided
 405 in table 1. For instance, by using analytic laws dependent on S_v and ϕ proposed in [50] for the Kelvin-cell
 406 ceramic samples, β_{eff} for the 80 % and 90 % porosities is equal to 3.13 cm^{-1} and 1.78 cm^{-1} , respectively.
 407 This suggests that radiation propagates more in the 90 % porosity samples than in the 80 % porosity
 408 samples. The same observation holds for the random-cell ceramic samples, see table 2 for the values of
 409 β_{eff} calculated according to the analytical formulations provided in [60];
- 410 • with respect to the topology, the radiation is most effective within the Kelvin-cell ceramic samples as
 411 it reported the maximal increase in $\Delta\bar{T}_z$, followed by the random-cell and then the cubic-cell ceramic
 412 samples;

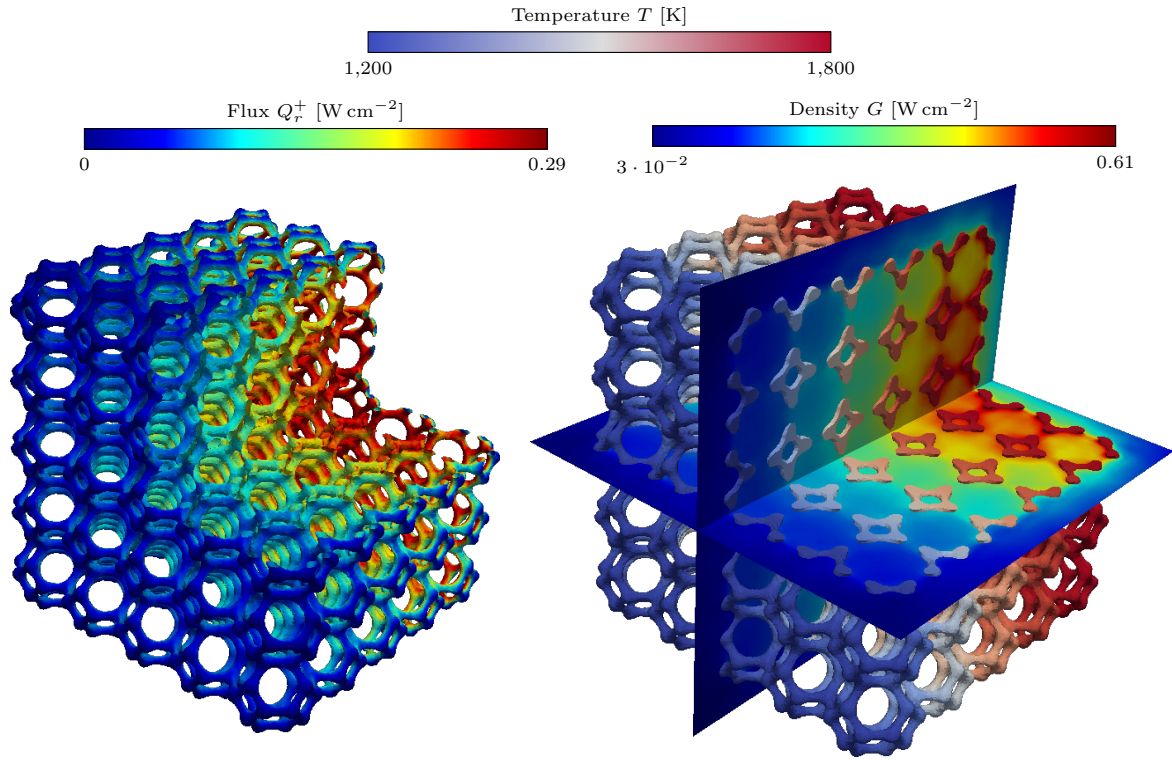


Figure 13: combined solution field visualizations acquired from conduction–radiation simulation of the SiC Kelvin-cell ceramic samples at 90 % porosity. Right: temperature field visualized for the solid part and radiative density field visualized for the orthogonal void cross-sections. Left: radiative heat flux field visualized for the solid part boundary.

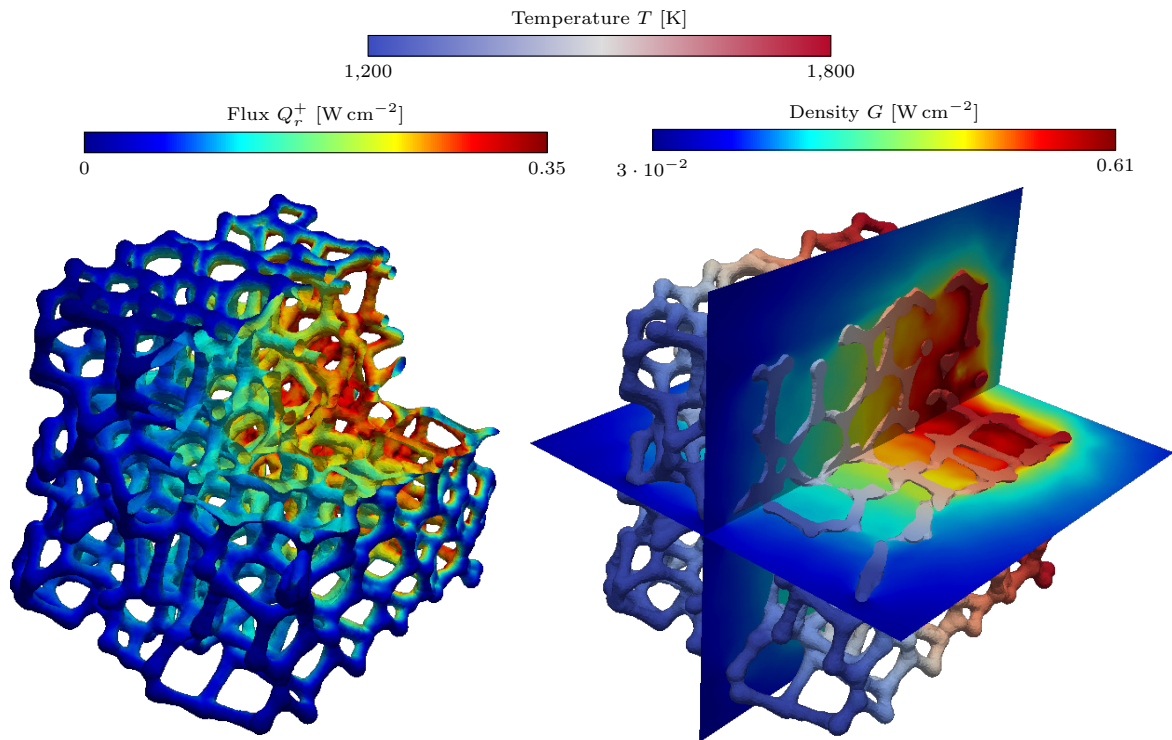


Figure 14: combined solution field visualizations acquired from conduction–radiation simulation of the SiC random-cell ceramic samples at 90 % porosity. Right: temperature field visualized for the solid part and radiative density field visualized for the orthogonal void cross-sections. Left: radiative heat flux field visualized for the solid phase boundary.

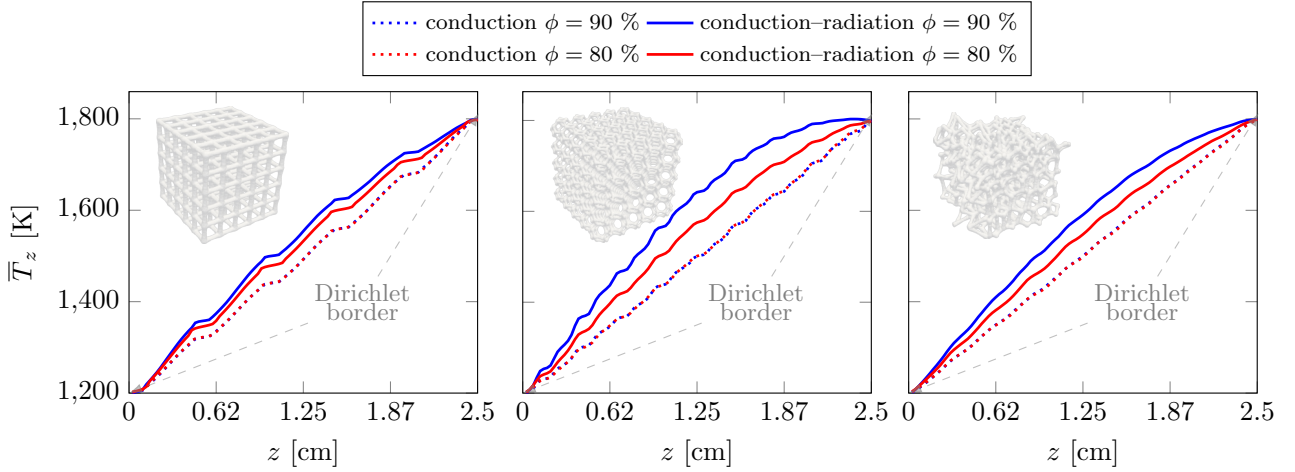


Figure 15: \bar{T}_z for conduction and conduction–radiation simulations for the cubic-cell (left), Kelvin-cell (middle), and random-cell (right) ceramics.

- 413 • Table 2 shows for all simulations $\max(\Delta\bar{T}_z)$, as well as the ordinates $L_{\max(\Delta\bar{T}_z)}$ that maximizes the
 414 difference. It is the greatest for the 90 % porosity Kelvin-cell ceramic sample, $\max(\Delta\bar{T}_z) = 140$ K. For all
 415 ceramic samples, the radiation propagation lengths increase when switching from 80 % to 90 % porosity
 416 samples.

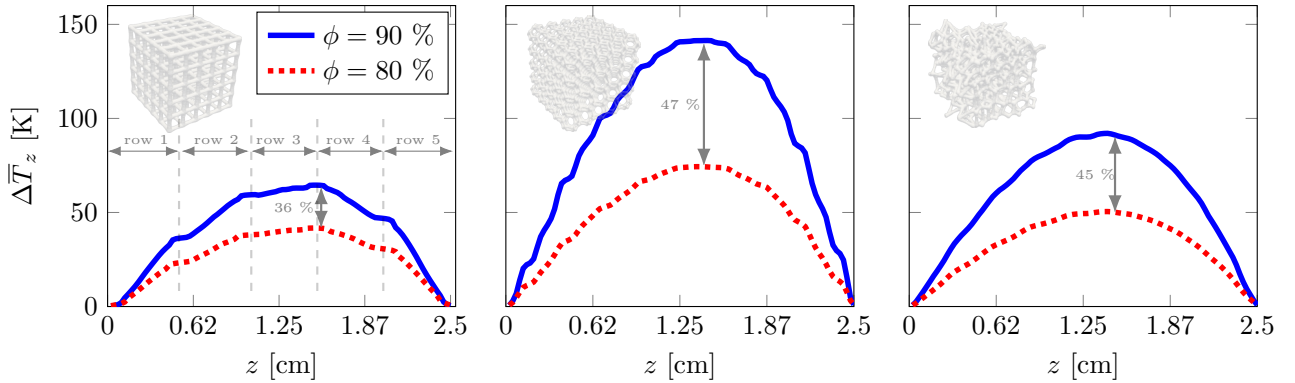


Figure 16: $\Delta\bar{T}_z$ for the cubic-cell (left), Kelvin-cell (middle), and random-cell (right) ceramics.

417 It is also possible to discuss the conduction–radiation results observed for the random-cell ceramics by
 418 using the conduction-to-radiation parameter $N = \lambda_{\text{eff}}\beta_{\text{eff}}/(4\sigma T_{\text{ref}}^3)$ [36], also referred as the Stark or the Planck
 419 number as defined by Howell et al. [37]. This parameter can be used if we consider that an upscaling approach
 420 may be applied with confidence [17, 60]. By using the analytical formulations proposed in [61] for the 80 %
 421 (resp. 90 %) porosity random-cell sample, λ_{eff} is equal to 0.02 (resp. 0.01) $\text{W cm}^{-1} \text{K}^{-1}$. These λ_{eff} and β_{eff}
 422 from table 2 lead to N equal to 0.29 (resp. 0.07). As found in the literature, for both porosities, $N \ll 10$.
 423 This highlights again that radiation plays a more important role than conduction [36]. Because the number of
 424 nonlinear iterations, k in table 1, is higher for solving the conduction–radiation problem with the 90 % than
 425 with the 80 % porosity random-cell ceramic, the coupling is likely tighter. A similar phenomenon when dealing
 426 with decreasing values of N was observed in [62].

427 To examine various properties and physical behaviors of macroporous cellular materials, the Kelvin cell–
 428 random cell analogy is often used to efficiently deal with multiphysics [63]. As such, Kelvin-cell structures are
 429 often used as representatives of random-cell structures, and numerical or experimental tests are performed on
 430 Kelvin-cell structures. To gauge the accuracy of such an assumption, we can apply here the same Kelvin-cell–
 431 random-cell analogy to our results from tests {2C,2E} and {2D,2F}. The analogy is true when only considering
 432 conduction, at least for our porosity range from 80 % to 90 %. Minor temperature variations (± 9 K) are present
 433 when comparing results at a constant porosity, see left-hand side fig. 17. However, the coupled conduction–
 434 radiation simulations show greater variations in temperatures, so that the Kelvin-cell–random-cell analogy does
 435 not hold. Note that $\max(\Delta\bar{T}_z)$ for the 90 % porosity Kelvin-cell ceramic is 1.5 times higher than that for the
 436 random-cell ceramic. It also suggests that the heating power of SiC Kelvin-cell ceramics is better than the one
 437 of random-cell ceramics within similar regimes (porosity and heating conditions).

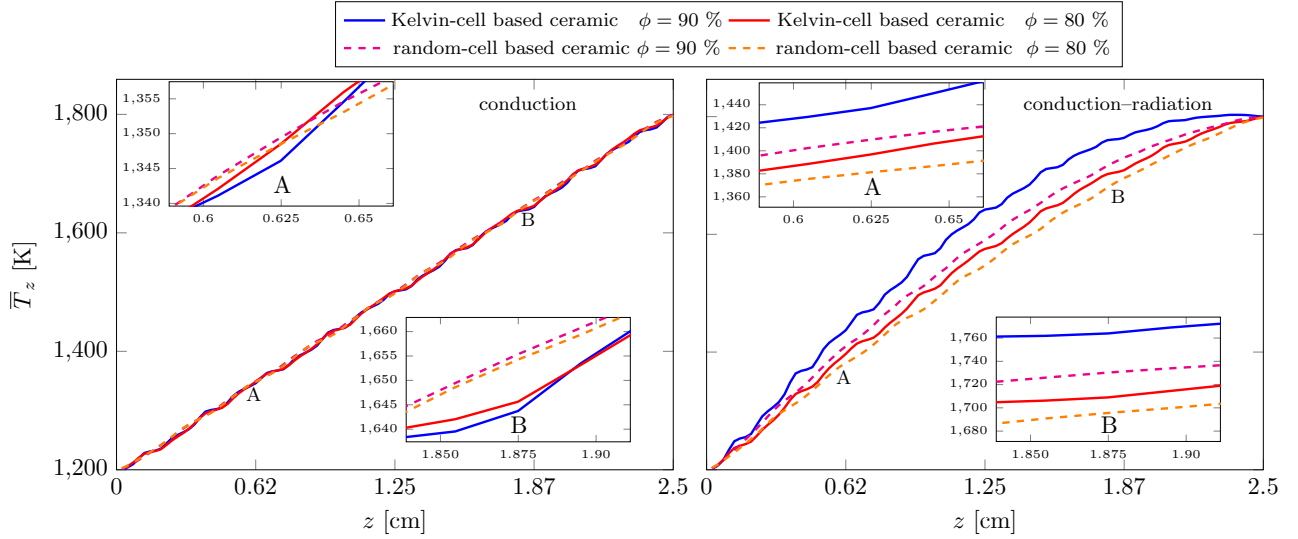


Figure 17: \bar{T}_z for the conduction (left) and the coupled conduction–radiation (right) simulations for the full-scale SiC-based Kelvin- and random-cell ceramics.

5. Conclusion

In this paper, a finite element model was established to solve the coupled conduction–radiation physics within SiC-based open-cell cellular ceramics operating at temperatures ranging from 1200 K to 1800 K. In particular, the vectorial finite element model was used for approximating the radiation physics, i.e., solving the radiative transfer equation, which was nonlinearly coupled to the standard finite element model for approximating the conduction physics, i.e., solving the heat conduction equation. These models were assembled together using a finite element domain-specific language, FreeFEM, and then solved with PETSc.

Specific numerical experiments were designed with the aim of highlighting the role of conduction–radiation coupling within the SiC-based open-cell cellular ceramic structures. More precisely, in these numerical experiments, the cubic-, Kelvin-, and random-cell cellular ceramic structures at both 80 % and 90 % porosities were investigated. Besides these full-scale simulations, the standalone cubic and Kelvin cells were also investigated.

To ensure comprehensive physics-based simulations compared to the conventional continuum-scale approaches that average the volumes, the geometries, and the properties, our numerical simulations were based on a discrete-scale approach involving realistic geometries with microstructure properties. Due to its important computational cost, the discrete-scale approach has mostly been used for modest mesh sizes when using deterministic radiation models. We presented results using detailed open-cell cellular ceramic geometries thanks to the efficient use of distributed-memory parallelism.

Radiative transfer, that forms a dominant part of conduction–radiation energy exchange within the SiC ceramics, was analyzed by means of radiation density and radiation heat flux, and by calculating the total absorbed radiation by the ceramic ligaments. It was revealed that the Kelvin-cell topology is favorable for maximizing the radiation gains when compared to the cubic- and the random-cell topology.

The data from our numerical experiments provides means for better understanding the role of radiation in coupled conduction–radiation physics within cellular ceramics. Our numerical data suggests that within the standalone or full-scale SiC structures operating at temperatures ranging from 1200 K to 1800 K, the radiation plays a dominant role. As such, it cannot be neglected while modeling such scenarios. Considering only conduction leads to an under prediction of the real temperature within the SiC cell ligaments. This effect was even more pronounced in the full-scale ceramics than in the standalone cells. To quantify the effect of the coupling, we compared the difference in mean temperatures.

The numerical experiments also suggest that the Kelvin-cell ceramics are, indeed, good representatives of random-cell ceramics when only considering conduction. However, the same cannot be said for coupled conduction–radiation, for which there are important mean temperature differences between the Kelvin-cell ceramics and the random-cell ceramics. Our results are furthermore coherent with upscaling approaches based on the use of the Stark or the Planck number – which is also known as the conduction-to-radiation parameter.

Changes in porosity had a considerable effect on the conduction–radiation coupling for all the SiC structures except the standalone SiC cubic cell. We observed that changing the porosity from 80 % to 90 % increased the radiative transfer, leading to a tighter coupling. As a side effect, the number of nonlinear iterations needed by our solver to reach convergence slightly increased.

The role of convection within macroporous ceramics has yet to be determined. Also, extending our numerical experiments to quantify the effect of conduction–radiation in semi-transparent materials, which adds refractions

477 alongside reflections, remains a challenge. This numerical work could be extended to applied studies where
478 cellular materials are used as host supports for conversion energy processes occurring at temperatures higher
479 than 1000 K.

480 Acknowledgments

481 The author M. A. Badri would like to thank IRT Jules Verne, Bouguenais, France (Institute in Research and
482 Technology in Advance Manufacturing Technologies for Composite, Metallic, and Hybrid Structures) for funding
483 his research during his whole Ph.D. thesis. The company Mersen, Gennevilliers, France, is also acknowledged for
484 its final financial contribution. The authors would like to thank Arnaud Biallais from SATT Ouest Valorisation,
485 France (currently working at Pixel Group, France) for his kind help with the genMat software. The authors also
486 thank the Institute of Intensive Computation, Centrale Nantes, France, for the access to LIGER. M. A. Badri,
487 Y. Favennec, and B. Rousseau would like to warmly thank Distinguished Professor Emeritus Michael F. Modest,
488 University of California, Merced, USA, and Professor Sophia Haussener, EPFL, Lausanne, Switzerland, for
489 fruitful and valuable discussions on the subjects of radiative transfer and porous material radiation. Finally,
490 the French Research Network ACCORT (GDR CNRS 3438), funded by CNRS, is also thanked for providing
491 high-level framework for scientific exchanges.

492 References

- 493 [1] L. Ferrari, M. Barbato, B. Esser, I. Petkov, M. Kuhn, S. Gianella, J. Barcena, C. Jimenez, D. Francesconi,
494 V. Liedtke, et al., Sandwich structured ceramic matrix composites with periodic cellular ceramic cores:
495 An active cooled thermal protection for space vehicles, *Composite Structures* 154 (2016) 61–68.
- 496 [2] A. Fuessel, H. Klemm, D. Boettge, F. Marschallek, J. Adler, A. Michaelis, Advancement of cellular
497 ceramics made of silicon carbide for burner applications, in: *IOP Conference Series: Materials Science and*
498 *Engineering*, 18, IOP Publishing, p. 182001.
- 499 [3] A. Kribus, Y. Gray, M. Grijnevich, G. Mittelman, S. Mey-Cloutier, C. Caliot, The promise and challenge
500 of solar volumetric absorbers, *Solar Energy* 110 (2014) 463–481.
- 501 [4] P. Furler, J. Scheffe, D. Marxer, M. Gorbar, A. Bonk, U. Vogt, A. Steinfeld, Thermochemical CO₂
502 splitting via redox cycling of ceria reticulated foam structures with dual-scale porosities, *Physical Chemistry*
503 *Chemical Physics* 16 (2014) 10503–10511.
- 504 [5] M. Nacken, L. Ma, S. Heidenreich, F. Verpoort, G. V. Baron, Development of a catalytic ceramic foam for
505 efficient tar reforming of a catalytic filter for hot gas cleaning of biomass-derived syngas, *Applied Catalysis*
506 *B: Environmental* 125 (2012) 111–119.
- 507 [6] A. Ortona, D. Trimis, V. Uhlig, R. Eder, S. Gianella, P. Fino, G. D’Amico, E. Boulet, C. Chazelas,
508 T. Grämer, et al., SiSiC heat exchangers for recuperative gas burners with highly structured surface
509 elements, *International Journal of Applied Ceramic Technology* 11 (2014) 927–937.
- 510 [7] M. A. Mendes, P. Goetze, P. Talukdar, E. Wertzner, C. Demuth, P. Rössger, R. Wulf, U. Gross, D. Trimis,
511 S. Ray, Measurement and simplified numerical prediction of effective thermal conductivity of open-cell
512 ceramic foams at high temperature, *International Journal of Heat and Mass Transfer* 102 (2016) 396–406.
- 513 [8] B. Dietrich, T. Fishedick, M. Wallenstein, M. Kind, Thermal conductivity of ceramic sponges at temper-
514 atures up to 1000 °C, *Special Topics & Reviews in Porous Media: An International Journal* 6 (2015).
- 515 [9] M. Pelanconi, M. Barbato, S. Zavattoni, G. Vignoles, A. Ortona, Thermal design, optimization and additive
516 manufacturing of ceramic regular structures to maximize the radiative heat transfer, *Materials & Design*
517 163 (2019) 107539.
- 518 [10] D. Y. Perraudin, S. Haussener, Numerical quantification of coupling effects for radiation-conduction heat
519 transfer in participating macroporous media: Investigation of a model geometry, *International Journal of*
520 *Heat and Mass Transfer* 112 (2017) 387–400.
- 521 [11] P. Colombo, Conventional and novel processing methods for cellular ceramics, *Philosophical Transactions*
522 *of the Royal Society A: Mathematical, Physical and Engineering Sciences* 364 (2005) 109–124.
- 523 [12] T. Fishedick, M. Kind, B. Dietrich, High temperature two-phase thermal conductivity of ceramic sponges
524 with stagnant fluid—experimental results and correlation including thermal radiation, *International Journal*
525 *of Thermal Sciences* 96 (2015) 1–11.

- 526 [13] C. C. Tseng, R. L. Sikorski, R. Viskanta, M. Y. Chen, Effect of foam properties on heat transfer in high
527 temperature open-cell foam inserts, *Journal of the American Ceramic Society* 95 (2012) 2015–2021.
- 528 [14] R. Coquard, D. Rochais, D. Baillis, Experimental investigations of the coupled conductive and radiative
529 heat transfer in metallic/ceramic foams, *International Journal of Heat and Mass Transfer* 52 (2009) 4907–
530 4918.
- 531 [15] R. Coquard, D. Baillis, J. Randrianalisoa, Homogeneous phase and multi-phase approaches for modeling
532 radiative transfer in foams, *International Journal of Thermal Sciences* 50 (2011) 1648–1663.
- 533 [16] W. Lipiński, J. Petrasch, S. Haussener, Application of the spatial averaging theorem to radiative heat
534 transfer in two-phase media, *Journal of Quantitative Spectroscopy and Radiative Transfer* 111 (2010)
535 253–258.
- 536 [17] S. Whitaker, *The Method of Volume Averaging*, volume 13, Springer Science & Business Media, 2013.
- 537 [18] M. A. Mendes, P. Talukdar, S. Ray, D. Trimis, Detailed and simplified models for evaluation of effective
538 thermal conductivity of open-cell porous foams at high temperatures in presence of thermal radiation,
539 *International Journal of Heat and Mass Transfer* 68 (2014) 612–624.
- 540 [19] Y. Li, X.-L. Xia, C. Sun, S.-D. Zhang, H.-P. Tan, Integrated simulation of continuous-scale and discrete-
541 scale radiative transfer in an open-cell foam made of semitransparent absorbing-scattering ceramics, *Journal*
542 *of Quantitative Spectroscopy and Radiative Transfer* 225 (2019) 156–165.
- 543 [20] Y. Li, X.-L. Xia, C. Sun, H.-P. Tan, J. Wang, Pore-level numerical analysis of the infrared surface temper-
544 ature of metallic foam, *Journal of Quantitative Spectroscopy and Radiative Transfer* 200 (2017) 59–69.
- 545 [21] M. A. Mendes, V. Skibina, P. Talukdar, R. Wulf, U. Gross, D. Trimis, S. Ray, Experimental validation of
546 simplified conduction–radiation models for evaluation of effective thermal conductivity of open-cell metal
547 foams at high temperatures, *International Journal of Heat and Mass Transfer* 78 (2014) 112–120.
- 548 [22] R. Coquard, D. Rochais, D. Baillis, Conductive and radiative heat transfer in ceramic and metal foams at
549 fire temperatures, *Fire Technology* 48 (2012) 699–732.
- 550 [23] J. Randrianalisoa, D. Baillis, Thermal conductive and radiative properties of solid foams: Traditional and
551 recent advanced modelling approaches, *Comptes Rendus Physique* 15 (2014) 683–695.
- 552 [24] M. Loretz, E. Maire, D. Baillis, Analytical modelling of the radiative properties of metallic foams: Contri-
553 bution of X-ray tomography, *Advanced Engineering Materials* 10 (2008) 352–360.
- 554 [25] D. Le Hardy, M. A. Badri, B. Rousseau, S. Chupin, D. Rochais, Y. Favennec, 3D numerical modelling
555 of the propagation of radiative intensity through a X-ray tomographed ligament, *Journal of Quantitative*
556 *Spectroscopy and Radiative Transfer* 194 (2017) 86–97.
- 557 [26] S. Cunsolo, D. Baillis, N. Bianco, V. Naso, M. Oliviero, Effects of ligaments shape on radiative heat transfer
558 in metal foams, *International Journal of Numerical Methods for Heat & Fluid Flow* 26 (2016) 477–488.
- 559 [27] V. Leroy, B. Goyeau, J. Taine, Coupled upscaling approaches for conduction, convection, and radiation in
560 porous media: theoretical developments, *Transport in Porous Media* 98 (2013) 323–347.
- 561 [28] P. Ferkl, R. Pokorný, J. Kosek, Multiphase approach to coupled conduction–radiation heat transfer in
562 reconstructed polymeric foams, *International Journal of Thermal Sciences* 83 (2014) 68–79.
- 563 [29] G. L. Vignoles, A hybrid random walk method for the simulation of coupled conduction and linearized
564 radiation transfer at local scale in porous media with opaque solid phases, *International Journal of Heat*
565 *and Mass Transfer* 93 (2016) 707–719.
- 566 [30] S. Guévelou, B. Rousseau, G. Domingues, J. Vicente, C. Caliot, Representative elementary volumes
567 required to characterize the normal spectral emittance of silicon carbide foams used as volumetric solar
568 absorbers, *International Journal of Heat and Mass Transfer* 93 (2016) 118–129.
- 569 [31] M. Scheffler, P. Colombo, *Cellular Ceramics: Structure, Manufacturing, Properties and Applications*, John
570 Wiley & Sons, 2006.
- 571 [32] S. Guévelou, B. Rousseau, G. Domingues, J. Vicente, A simple expression for the normal spectral emittance
572 of open-cell foams composed of optically thick and smooth struts, *Journal of Quantitative Spectroscopy*
573 *and Radiative Transfer* 189 (2017) 329–338.

- 574 [33] M. A. Badri, P. Jolivet, B. Rousseau, S. Le Corre, H. Dignonnet, Y. Favennec, Vectorial finite elements for
575 solving the radiative transfer equation, *Journal of Quantitative Spectroscopy and Radiative Transfer* 212
576 (2018) 59–74.
- 577 [34] M. A. Badri, P. Jolivet, B. Rousseau, Y. Favennec, High performance computation of radiative transfer
578 equation using the finite element method, *Journal of Computational Physics* 360 (2018) 74–92.
- 579 [35] W. Fiveland, Discrete-ordinates solutions of the radiative transport equation for rectangular enclosures,
580 *Journal of Heat Transfer* 106 (1984) 699–706.
- 581 [36] M. F. Modest, *Radiative Heat Transfer*, Academic Press, 2013.
- 582 [37] J. R. Howell, M. P. Menguc, R. Siegel, *Thermal Radiation Heat Transfer*, CRC Press, 2010.
- 583 [38] L. Ruan, M. Xie, H. Qi, W. An, H. Tan, Development of a finite element model for coupled radiative
584 and conductive heat transfer in participating media, *Journal of Quantitative Spectroscopy and Radiative*
585 *Transfer* 102 (2006) 190–202.
- 586 [39] M. Ghattassi, J. R. Roche, F. Asllanaj, M. Boutayeb, Galerkin method for solving combined radiative and
587 conductive heat transfer, *International Journal of Thermal Sciences* 102 (2016) 122–136.
- 588 [40] D. Le Hardy, Y. Favennec, B. Rousseau, F. Hecht, Specular reflection treatment for the 3D radiative
589 transfer equation solved with the discrete ordinates method, *Journal of Computational Physics* 334 (2017)
590 541–572.
- 591 [41] M. A. Badri, Efficient finite element strategies for solving the radiative transfer equation, Ph.D. thesis,
592 Université de Nantes, 2018.
- 593 [42] M. A. Badri, P. Jolivet, B. Rousseau, Y. Favennec, Preconditioned Krylov subspace methods for solving
594 radiative transfer problems with scattering and reflection, *Computers & Mathematics with Applications*
595 77 (2019) 1453–1465.
- 596 [43] A. N. Brooks, T. J. Hughes, Streamline upwind/Petrov-Galerkin formulations for convection dominated
597 flows with particular emphasis on the incompressible Navier-Stokes equations, *Computer Methods in*
598 *Applied Mechanics and Engineering* 32 (1982) 199–259.
- 599 [44] M. Avila, R. Codina, J. Principe, Spatial approximation of the radiation transport equation using a
600 subgrid-scale finite element method, *Computer Methods in Applied Mechanics and Engineering* 200 (2011)
601 425–438.
- 602 [45] M. Sakami, A. Charette, V. Le Dez, Application of the discrete ordinates method to combined conductive
603 and radiative heat transfer in a two-dimensional complex geometry, *Journal of Quantitative Spectroscopy*
604 *and Radiative Transfer* 56 (1996) 517–533.
- 605 [46] G. Karypis, K. Schloegel, V. Kumar, Parnetis: Parallel graph partitioning and sparse matrix ordering
606 library, Version 1.0, Dept. of Computer Science, University of Minnesota (1997) 22.
- 607 [47] F. Hecht, New development in FreeFem++, *Journal of Numerical Mathematics* 20 (2012) 251–266.
- 608 [48] S. Balay, S. Abhyankar, M. F. Adams, J. Brown, P. Brune, K. Buschelman, L. Dalcin, A. Dener, V. Eijkhout,
609 W. D. Gropp, D. Karpeyev, D. Kaushik, M. G. Knepley, D. A. May, L. C. McInnes, R. T. Mills, T. Munson,
610 K. Rupp, P. Sanan, B. F. Smith, S. Zampini, H. Zhang, H. Zhang, PETSc Web page, [https://www.mcs.
611 anl.gov/petsc](https://www.mcs.anl.gov/petsc), 2019.
- 612 [49] S. G. Müller, R. Eckstein, J. Fricke, D. Hofmann, R. Hofmann, R. Horn, H. Mehling, O. Nilsson, Experi-
613 mental and theoretical analysis of the high temperature thermal conductivity of monocrystalline SiC, in:
614 *Materials Science Forum*, volume 264, Trans Tech Publ, pp. 623–626.
- 615 [50] S. Cunsolo, R. Coquard, D. Baillis, W. K. Chiu, N. Bianco, Radiative properties of irregular open cell solid
616 foams, *International Journal of Thermal Sciences* 117 (2017) 77–89.
- 617 [51] W. E. Lorensen, H. E. Cline, Marching cubes: A high resolution 3D surface construction algorithm, in:
618 *ACM Siggraph Computer Graphics*, volume 21, ACM, pp. 163–169.
- 619 [52] C. Dapogny, C. Dobrzynski, P. Frey, Three-dimensional adaptive domain remeshing, implicit domain
620 meshing, and applications to free and moving boundary problems, *Journal of Computational Physics* 262
621 (2014) 358–378.

- 622 [53] C. Dobrzynski, P. Frey, Anisotropic Delaunay mesh adaptation for unsteady simulations, in: Proceedings
623 of the 17th International Meshing Roundtable, Springer, 2008, pp. 177–194.
- 624 [54] C. Geuzaine, J. F. Remacle, Gmsh: A 3-D finite element mesh generator with built-in pre-and post-
625 processing facilities, International Journal for Numerical Methods in Engineering 79 (2009) 1309–1331.
- 626 [55] M. A. Badri, Y. Favennec, P. Jolivet, S. Le Corre, B. Rousseau, A parallel implicit mixed-FEM solution
627 for complex domain radiative transfer problems using immersed meshes, in: Proceedings of Computational
628 Thermal Radiation in Participating Media VI Eurotherm Seminar No. 110, 2018.
- 629 [56] P. R. Amestoy, I. S. Duff, J.-Y. LExcellent, J. Koster, MUMPS: a general purpose distributed memory
630 sparse solver, in: International Workshop on Applied Parallel Computing, Springer, pp. 121–130.
- 631 [57] Q.-H. Deng, G.-F. Tang, Numerical visualization of mass and heat transport for conjugate natural con-
632 vection/heat conduction by streamline and heatline, International Journal of Heat and Mass Transfer 45
633 (2002) 2373–2385.
- 634 [58] V. Costa, Unified streamline, heatline and massline methods for the visualization of two-dimensional
635 heat and mass transfer in anisotropic media, International Journal of Heat and Mass Transfer 46 (2003)
636 1309–1320.
- 637 [59] U. Ayachit, The ParaView Guide: A Parallel Visualization Application, Kitware, Inc., 2015.
- 638 [60] S. Guevelou, B. Rousseau, G. Domingues, J. Vicente, C. Caliot, G. Flamant, Evolution of the homogenized
639 volumetric radiative properties of a family of α -SiC foams with growing nominal pore diameter, Journal
640 of Porous Media 18 (2015).
- 641 [61] A. Öchsner, G. E. Murch, M. J. de Lemos, Cellular and Porous Materials: Thermal Properties Simulation
642 and Prediction, John Wiley & Sons, 2008.
- 643 [62] S. C. Mishra, C. H. Krishna, M. Y. Kim, Analysis of conduction and radiation heat transfer in a 2-
644 D cylindrical medium using the modified discrete ordinate method and the lattice Boltzmann method,
645 Numerical Heat Transfer, Part A: Applications 60 (2011) 254–287.
- 646 [63] G. Contento, M. Oliviero, N. Bianco, V. Naso, The prediction of radiation heat transfer in open cell
647 metal foams by a model based on the Lord Kelvin representation, International Journal of Heat and Mass
648 Transfer 76 (2014) 499–508.